Quaternary Geochronology 73 (2022) 101406

Contents lists available at ScienceDirect

Quaternary Geochronology

journal homepage: www.elsevier.com/locate/quageo

Research paper

Rock surface and sand-sized sediment quartz dating using optically stimulated luminescence of a Middle-to-Upper Palaeolithic sequence at the Bordes-Fitte rock shelter (Les Roches d'Abilly, Central France)

Trine H. Freiesleben [a,*], Kristina J. Thomsen [a], Andrew S. Murray [b], Reza Sohbati [a], Mayank Jain [a], Søren Hvidt [c], Bo Jakobsen [d], Thierry Aubry [e]

[a] Department of Physics, Technical University of Denmark, DTU Risø, Campus, Denmark
[b] Nordic Laboratory for Luminescence Dating, Department of Geoscience, Aarhus University, and Department of Physics, Technical University of Denmark, DTU Risø, Campus, Denmark
[c] Department of Science, Systems and Models, Roskilde University, Denmark
[d] "Glass and Time", IMFUFA, Department of Science and Environment, Roskilde University, Postbox 260, DK-4000, Roskilde, Denmark
[e] Côa Parque, Fundação para a Salvaguarda e Valorização do Vale do Côa, Rua do Museu, 5150-610 Vila Nova de Foz Côa, Portugal

ARTICLE INFO

Keywords:
Rock surface burial dating
Rock slices
Dose rate modelling
Multi-grain quartz OSL dating
Middle-to-Upper Paleaeolithic transition
Châtelperronian

ABSTRACT

In this study, we use optically stimulated luminescence (OSL) to establish a robust absolute chronology for the lower part of the stratigraphic record at "Les Roches d'Abilly", an important Palaeolithic site in Central France. There, lithic assemblages recording the Middle-to-Upper Palaeolithic transition and the behaviour of Neanderthal and Anatomically Modern Human populations are preserved. At the Bordes-Fitte rock shelter, part of "Les Roches d'Abilly", the archaeo-stratigraphic record has been sealed and preserved by the collapse of the shelter roof and this site has provided important data on the timing of human occupations and Middle-to-Upper Palaeolithic transition in this region.

Here, we first obtain burial ages using standard multi-grain quartz techniques on sand-sized sediment grains and then investigate the information available in blue-stimulated luminescence-depth profiles into the surfaces of four quartz-rich cobbles found in the sedimentary record below the various collapses of the shelter roof. These profiles show qualitative evidence for past daylight exposure and a single burial event, allowing the data to be analysed quantitatively using a multiple-event mathematical model. Based on the results of this modelling, it is concluded that at least part of the cobble surfaces were well-bleached at burial and thus that estimated rock surface burial ages are unlikely to be significantly affected by incomplete bleaching. However, it appears that not all cobble surfaces were well-bleached, demonstrating the importance of only using surface doses derived from those cobble layers that can be shown to have been well-bleached at burial. The rock-surface burial ages of the most recent burial event are consistent with the quartz OSL ages derived from the surrounding sediments, giving burial ages of ~50 ka. The OSL ages are consistent with previously published ^{14}C age control, although a single ^{14}C age (uncalibrated age of $41,900 \pm 1,500$ yr BP) of a lower unit may underestimate the OSL ages. This study provides a reliable absolute OSL chronology for the Bordes-Fitte rock shelter constraining the Middle-to-Upper Palaeolithic transition to occur between 44±2 ka and 48±3 ka ago (at the 68% confidence level).

1. Introduction

In France and northern Iberia the transition from the Middle to the Upper Palaeolithic took place about 40 to 50 ka ago and records the replacement of the Neanderthals in favour of Anatomically Modern Humans (AMH; e.g. Aubry et al. 2012, Higham et al. 2014). In this transitional period, Mousterian industries (attributed to Neanderthals) were replaced by new so-called transitional industries (e.g. the Châtelperronian in France and Cantabrian in Spain) incorporating elements from both Middle Palaeolithic (Neanderthals) and subsequent Upper

* Corresponding author.
E-mail address: trihof@dtu.dk (T.H. Freiesleben).

https://doi.org/10.1016/j.quageo.2022.101406
Received 20 February 2022; Received in revised form 5 September 2022; Accepted 7 October 2022
Available online 13 October 2022

Palaeolithic (AMH) industries (Talamo et al., 2020). The identity of the creators (Neanderthal or AMH) of the Châtelperronian transitional industry is still debated (e.g. Higham et al., 2010; Hublin et al., 2012; Gravina et al., 2018). Such identification is key to understanding whether or not these two human populations co-existed in Western Eurasia and if so had cultural exchange. Until recently, these European transitional industries had only been found located stratigraphically between Middle and Upper Paleolitic layers, but new data from Grotte Mandrin (France) show an alternating transitional (argued to be of AMH origin) and Middle Palaeolithic industries at 54±3 ka ago and these data are used to argue that there has been no major interactions between the two human populations (Slimak et al., 2022). Nonetheless, it remains important to establish site specific reliable absolute chronologies for the transitional industries to allow comparison between sites at a regional scale and so better constrain and understand when the transition between the Middle and Upper Paleolithic took place.

The archaeological site of les Roches d'Abilly is a complex of loci discovered in 1949 and located in the Creuse valley at the southern limit of the Touraine region in Central France. Between 2007 and 2014, excavations were carried out at several locations along the ~300 m long cliff where large collapsed slabs have preserved deposits containing Middle and Upper Palaeolithic stone tools and faunal remains. When the sections of the roof of the rock shelter collapsed, they preserved nine geoarchaeological units (GFUs) containing items attributed to the Middle Palaeolithic (Neanderthals), Châtelperronian (unknown origin), Aurignacian, Solutrean, Badegoulian and Magdalenian (AMH). These artefacts are related to the transition period from a Neanderthal to an AMH population (Aubry et al., 2012, 2014). The site contains an exceptional stratigraphy from the Middle to the Upper Palaeolithic with the Châtelperronian industry inter-stratified. Given the implications for the timing of the Middle to Upper Palaeolithic lithic technological transition, establishing a reliable chronology is considered to be crucial.

The main purpose of this study is to establish a reliable absolute chronology for the Bordes-Fitte rock shelter; particularly for the sediment units containing Middle Palaeolithic and Châtelperronian artefacts. To achieve this, we apply well-established multi-grain quartz OSL techniques to sand-sized sedimentary grains (henceforth referred to as sediment; e.g. Duller, 2008a; Murray et al., 2021) together with rock surface luminescence dating (RSLD) OSL techniques (e.g. Liritzis, 2011; Sohbati, 2013) to clast size cobbles. Optically stimulated luminescence (OSL) dating is a well-established absolute chronological method that determines the time since sedimentary grains were last exposed to daylight, i.e.it determines the burial age (Aitken, 1998). One of the main assumptions in OSL dating is that the sediment was sufficiently exposed to daylight to have any prior luminescence signal completely reset at burial. This assumption can to some degree be tested by comparison of ages derived from signals with different bleaching rates,(usually quartz OSL and K-rich feldspar IRSL (Murray et al., 2012), or in some cases by single-grain quartz OSL dating (e.g. Olley et al., 1999; Thomsen et al., 2007). More recently, OSL has also been applied to the dating of rock surfaces. One considerable advantage of rock surface luminescence dating (RSLD) compared to the dating of buried sediments is that rock surfaces preserve both qualitative and potentially quantitative information about the duration of past daylight exposure and burial events (see e.g. Liritzis, 1994; Habermann et al., 2000; Polikreti et al., 2002; Sohbati et al., 2012b) and thus provide an internal sample-specific check on the degree of resetting, which is key to accurate RSLD burial age estimation. Estimating which layers to include in the burial dose estimation can be done either qualitatively by including layers giving a "flat" luminescence level near the surface, (e.g. Habermann et al., 2000; Polikreti et al., 2002, 2003; Greilich et al., 2005; Vieillevigne et al., 2006; Vafiadou et al., 2007; Liritzis et al., 2010; Liritzis, 2011; Simms et al., 2011; Sohbati et al., 2011; Galli et al., 2014; Liritzis and Vafiadou, 2015; Liritzis et al., 2015, 2016, 2018, 2019; Puttagan et al., 2019; Galli et al., 2020; Gliganic et al., 2021) or quantitatively by identifying well-bleached layers using modelling (e.g. Laskaris and Liritzis, 2011; Sohbati et al., 2012b; Chapot et al., 2012). Here we use the multiple event model proposed by Freiesleben et al. (2015), which provides analytical solutions based on first-order charge detrapping and trapping kinetics for sequential exposure and burial events, i.e.it allows the prediction of the pre-burial profile and thus a quantitative identification of the well-bleached depth (e.g. Sohbati et al., 2015; Jenkins et al., 2018; Rades et al., 2018; al Khasawneh et al., 2018, 2019; Sellwood et al., 2019; Souza et al., 2019; Bailiff et al., 2021; Souza et al., 2021; Ageby et al., 2021; Cunningham et al., 2022; Ishii et al., 2022; al Khasawneh et al., 2022). A similar model to fit luminescence burial profiles was also proposed by Liritzis et al. (2017) using a cumulative log-normal distribution for exposure events (Laskaris and Liritzis, 2011).

A further potential advantage of RSLD compared to sediment OSL is that rock surfaces from larger clasts, such as cobbles, are more likely to have been well-bleached at burial than individual sand-sized sediment grains, because in any transport/mixing process the former are more likely to be found at the surface (Rosato et al., 1987) and so be exposed to daylight. Cobbles are internally unaffected by post-depositional mixing, because of the nature of the consolidated rock matrix, and will, in most burial environments, be correctly associated with the burial context as they are less likely to be mobilised after deposition than sand-sized sediment grains. A further advantage of RSLD compared to standard sediment dating concern the estimation of dose rate. In most settings, the dose rate contribution from the external sediment matrix is less than 10% just 2–3 mm into the rock surface (Jenkins et al., 2018), and thus any uncertainties arising from e.g. water content history, radon gas escape and other time-dependent phenomena, are negligible.

In this study, we derive 15 standard multi-grain sediment OSL ages and compare them to blue stimulated RSLD burial ages derived for four fist-sized cobbles found in the sedimentary sequence. Final quantitative OSL RSLD burial ages are derived using the multiple event model (Freiesleben et al., 2015). The OSL ages (both sediment and rocks) are compared to independent age control provided by AMS ^{14}C (Aubry et al., 2012) for two of the lithostratigraphic units.

2. Stratigraphy, current chronology and sampling

The Bordes-Fitte rock shelter contains a 2.5 metre thick sequence of sedimentary deposits composed of 9 lithostratigraphic units (GFU) containing Middle, Châtelperronian and Early Upper Palaeolithic artefacts. These units are interpreted in terms of sedimentary dynamics as near-surface sedimentary facies with vertical and lateral variations, all within a context dominated by run-off and sediment slope-wash, coupled with periods of alluvial and lacustrine deposition (Aubry et al., 2014). Lithic remains recovered in GFU A and B have yielded a small assemblage of flakes obtained from large recurrent centripetal or preferential Levallois cores (Neanderthal). The lithic assemblage from GFU C has been produced through a recurrent uni- and bi-directional convergent or centripetal recurrent Levallois method (Neanderthal). GFU D is divided into three sub-layers, and about 95% of the lithic assemblage was recovered in sub-layer GFU D2. The GFU D1 lithic assemblage has been obtained by Levallois recurrent and lineal methods (Neanderthal). Tools on flakes produced by the Discoidal reduction scheme (Neanderthal) and Châtelperronian backed points on blades (unknown makers) have been recovered in GFU D2. Sub-layer GFU D3, at the top of the unit, is almost sterile, probably indicating a break in human occupation. Aurignacian blade and bladelet production characterised the finds in GFU E (AMH). In GFU F, Solutrean bifacial thinning flakes, bifacial preforms and several fragments of laurel-leaves and Badegoulian have been found (AMH). Technology, refitting studies and taphonomy of lithic artefacts have shown that the Discoidal flake production and Châtelperronian blade production recovered in GFU D2 result from successive occupations, separated by wall and roof

collapse events, and affected by successive natural post-depositional displacement processes. Aubry et al. (2014) showed that lithic artefacts recovered in GFU D2, derived from blade production (Châtelperronian) overlie those that relate to the Discoidal method (Neanderthal).

Given the technological variability of the lithic assemblage (Discoidal and Châtelperronian Blade production) recovered in GFU D2 and the implications for the timing of the Middle to Upper Palaeolithic lithic technological transition, it is considered important to establish a reliable chronology. Previously, Aubry et al. (2012, 2020) published radiocarbon (^{14}C) AMS ages for four GFU levels (F, E, D2 and D1) on antler, bone and tooth obtained using the ultra-filtration protocol considered to be reliable (Thomsen et al., 2016). Here we re-calibrate these ^{14}C ages using OxCal v.4.4 and IntCal20 (Reimer et al., 2020) and obtain calibrated radiocarbon ages (at 95% confidence) of: 23.2–22.6 ka cal BP (GFU F), 41.4–37.4 kar cal BP (GFU E), 45.1–41.5 ka cal BP (GFU D2, n=5[1]) and 48.4–42.7 ka cal BP (GFU D1).

Thomsen et al. (2016) reported four multi-grain quartz OSL ages[2] of 22.4±1.2 ka (GFU F, expected to be consistent with 23.2–22.6 ka cal BP), 28.1±1.6 ka (GFU F, expected to be younger than 41.4–37.4 ka cal BP but older than 23.2–22.6 ka cal BP), 46±2 ka and 42±2 ka (both GFU D2, expected to be consistent with 45.1–41.5 ka cal BP). Thus, these multi-grain quartz OSL ages were in good agreement with the independent ^{14}C age control and also with OSL ages obtained using single-grain quartz and multi-grain K-rich feldspar measurements (Thomsen et al., 2016).

In 2013, 15 additional sediment samples containing sand-sized grains and four cobbles were sampled from the Bordes-Fitte rock shelter. Sediment samples (TA2247-61) were taken by inserting steel tubes (ø=5 cm, length=20 cm) into cleaned sections. These samples were taken as follows: one from GFU B (TA2247), four from GFU C (TA2248-51), one from the border between GFU C and D1 (TA2252), 4 from GFU D1 (TA2253-56), one from GFU D2 (TA2257) and three from GFU D3 (TA2258-61). Eight of the samples were positioned less than 15 cm away from bedrock/rock fall (see Table 1) and so a piece of bedrock (TA2262) was sampled to allow correction for non-uniformity in the gamma radiation field.

The buried cobbles (TA2265-68, TA2265 from GFU D1 and the remaining three from D2, see Fig. 1) were dug out of the cleaned sections and immediately placed in light-tight bags after marking the orientation of the cobbles in the section, i.e.top, bottom, out and in. Three of the cobbles (TA2265-67) were partly (on one side) exposed to daylight for about one month after excavation but prior to sampling. These recently light-exposed parts (facing outwards) were not used in the measurements reported here. The dimensions of the cobbles were ~ 12 × 12 × 4 cm^3 and they are either bio-calcirudite, calcarenite or harder silicified limestone (Aubry et al., 2012).

3. Experimental details

3.1. Sample preparation

The sediment samples (marked as red dots in Fig. 1) were prepared under subdued red-orange light following standard procedures; ~5 cm of the ends of each sample were removed as a consequence of possible light exposure during sampling. This sediment was used for radionuclide concentration and water content measurements. Quartz was extracted from the sediment in the inner part of each sample tube by sieving (180–250 μm), cleaning using HCl and H_2O_2, heavy liquid separation (ρ = 2.58 g cm^{-3}) and etching in 40% HF (Aitken, 1985).

The cobbles were also prepared under subdued red-orange light. Cores of ~10 mm in diameter and ~40 mm long, were drilled using a water-cooled diamond-tipped core drill. The cores were then cut into ~1.2 mm thick slices with a 0.3 mm thick water-cooled diamond-tipped wafer blade mounted on a Buehler IsoMet low-speed precision saw to give a known net slice spacing of ~1.5 mm. The cobbles studied here were visually homogeneous quartz-rich carbonate-cemented sandstone with friable surfaces; particularly cobbles TA2266 and -67. In order to avoid any effect of crushing on the luminescence signal and to produce and preserve the in situ grain size information (Sohbati, 2013), we first etched the slices in 10% HCl for one hour to remove calcium carbonate. At the end of this stage, the slices were still mostly intact, presumably due to binding by amorphous silica resistant to HCl. We then placed the slices in concentrated HF for one hour to further disaggregate the slices and dissolve any feldspar grains. By the end of this treatment the grains had completely separated from each other. Any residual fluoride contamination from the HF treatment was removed using a 10% HCl solution for 40 min. The washed and dried grains were sieved to the size range 63-300 μm.

Table 1
Sediment sample locations relative to bedrock measured from the centre of the sample tube to the bedrock surface. The distances have been used as input to the dose rate modelling (see Section 4.2). "Depth" is the burial depth, "H" is the horizontal distance to bedrock, "V_{above}" and "V_{below}" are the vertical distances to bedrock or shelter roof lying below and above the samples, respectively.

Sample	Depth (cm)	H (cm)	V_{above} (cm)	V_{below} (cm)
TA2247	221	12	>30	8
TA2248	205	9	>30	24
TA2249	213	>30	12	>30
TA2250	197	>30	12	>30
TA2251	181	16	90	11
TA2252	168	23	74	12
TA2253	160	48	66	19
TA2254	154	42	60	25
TA2255	159	29	65	11
TA2256	153	54	14	63
TA2257	138	54	21	56
TA2258	127	54	28	48
TA2259	122	54	33	43
TA2260	115	21	44	30
TA2261	108	23	59	17

3.2. Measurement facilities

All luminescence measurements were made using Risø TL/OSL readers equipped with blue (λ=470 nm, ~80 mW cm^{-2}) and infrared (IR, λ=870±40 nm, ~130 mW cm^{-2}) stimulation light sources. The emitted luminescence was detected using EMI 9635QA photomultipliers through 7.5 mm thick Hoya U-340 glass filters. Beta irradiation used calibrated ^{90}Sr/^{90}Y sources mounted on the readers (Bøtter-Jensen et al., 2010; Hansen et al., 2015).

Bulk radionuclide concentrations were measured using high-resolution gamma spectrometry (Murray et al., 1987, 2018). The cobble and sediment samples were dried at 50 °C, then pulverised and homogenised. The sediment samples were heated to 450 °C for 24 h to remove any organic matter. To prevent radon loss and to provide a reproducible counting geometry the materials were cast in wax. The cast samples were stored for at least three weeks to allow ^{222}Rn to reach equilibrium with its parent ^{226}Ra before measurement (Murray et al., 1987). The measured concentrations were converted to infinite matrix dose rates using the conversion and grain size attenuation factors of Guérin et al. (2011b, 2012), respectively (see Cresswell et al. (2018, 2019) for a comparison of conversion factors derived by different authors). An internal quartz alpha dose rate of 0.020 ± 0.010 Gy ka^{-1} was assumed, consistent with Vandenberghe et al. (2008). Cosmic ray dose rates were calculated following Prescott and Hutton (1994) and current burial depths; an uncertainty of 5% was assumed. The long term water content was taken to be 0% and 5% for the cobbles and sandy sediments, respectively. An uncertainty of 4% on the water content was assumed.

[1] Note that the range given for the radiocarbon ages for GFU D2 is the maximum and minimum for all 5 ^{14}C ages calibrated individually.

[2] OSL ages are generally reported at the 68% confidence level.

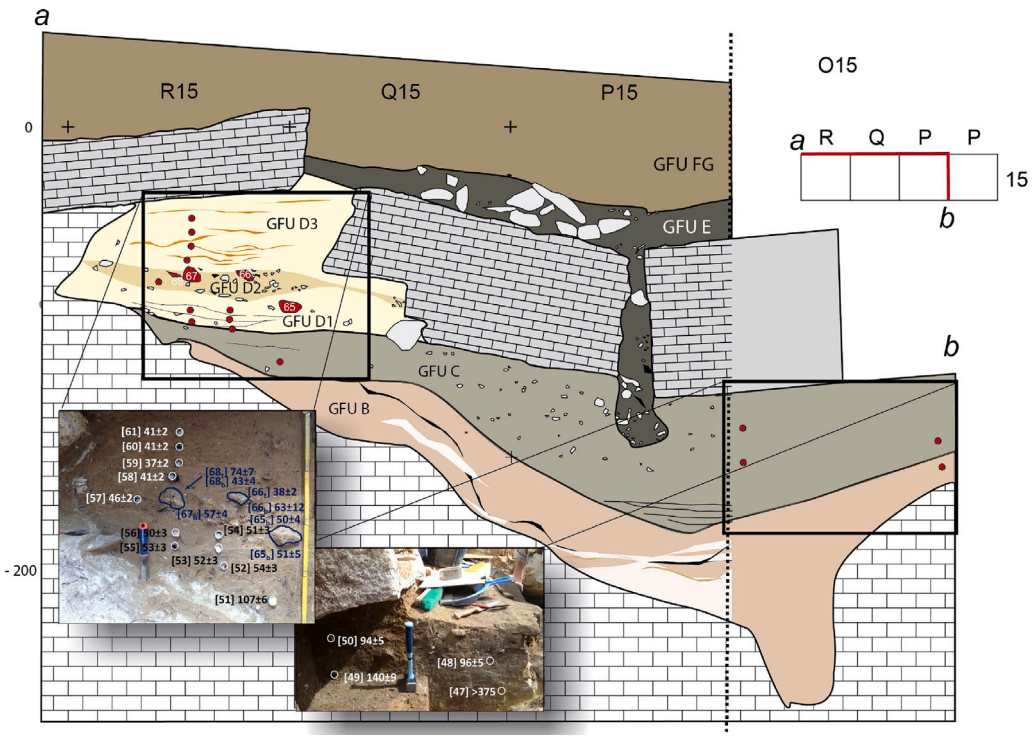

Fig. 1. Cross-section of part of the Bordes-Fitte rock shelter from where the OSL (Sediment: TA2247-61 and rock: TA2265-68) samples were taken. Sampling positions are indicated by red circles (sediment) or contours (rocks). Sampling photographs are shown inset. Sediment sample locations are indicated by white circles and rock samples are shown with dark blue outlines. Here the last two digits of the sample number are indicated in square brackets followed by the burial age in ka. One rock [65] was collected from GFU D1, whereas the other three were collected from GFU D2. Note that rock sample [68] is not directly visible in the Figure as it was buried behind rock [67]. For the rock samples the ages given are derived from profiles determined to be well-bleached (see Section 5.5.2 and Table 5). Rock ages are given both for top (e.g.[66$_t$]) and bottom (e.g.[66$_b$]) of the individual cobbles, except for rock sample [67] where surface slices from the top side could not be obtained. The grid references given in the top part of the figure (i.e. "R15") were used to localise the archaeological remains in 3D.

3.3. OSL measurements

All OSL measurements presented here were made using the single-aliquot regenerative-dose (SAR) procedure (Murray and Wintle, 2000) with blue light stimulation for 100 s at 125 °C (to avoid significant build-up of photo-transferred TL (PTTL) in the 110 °C peak). To monitor for isothermal signals blank channels were inserted before and after OSL stimulation. No significant isothermal signals were observed (see Figs. 5 and 6). For both sediments and rocks, early background subtraction (Ballarini et al., 2007) was used to maximise the fast-component contribution in the OSL signal used for calculations. Between each SAR cycle a 280 °C blue stimulation for 100 s was inserted to minimise potential recuperation effects (Murray and Wintle, 2003). Equivalent dose estimation is based on a minimum of three sensitivity corrected regeneration points (L_x/T_x), a recuperation point and a recycling point. Individual dose response curves (DRC) have been fitted using a single saturation exponential function passing through the origin (i.e. $y = A \times [1 - \exp(-x/D_c)]$, where y is the sensitivity corrected OSL response, L_x/T_x, A is the saturation value and the constant D_c is a measure of the curvature of the DRC) and equivalent doses (D_e) derived by interpolation of the sensitivity corrected natural signal (L_n/T_n) on the individual DRCs. Average equivalent dose values have been calculated using an unweighted arithmetic mean (Guérin et al., 2017) and the quoted uncertainty is the standard error (at 68% confidence). We do not apply rejection criteria based on IR depletion ratio, recycling ratio or recuperation value on an aliquot specific basis as there appears to be no correlation with equivalent dose and scatter (see Section 5.1.1). However, we use the InterQuartile Rejection (IQR) criterion (Medialdea et al., 2014) to identify and reject individual dose values more than 1.5 interquartile ranges above the upper quartile (75 percent), or below the lower quartile (25 percent). The effect of applying this criterion is examined in Section 5.3.

3.3.1. Sediment quartz OSL measurements

The OSL measurements of quartz sand extracted from sediment samples used a double SAR procedure (Banerjee et al., 2001) in which an IR stimulation at 50 °C for 100 s was inserted immediately before the blue light stimulation. Unless otherwise mentioned, the sediments were measured using a preheat of 260 °C (held for 10 s), a cutheat of 220 °C and a test dose of 50 Gy. The signal was summed over the initial ~0.3 s of stimulation (the blue light power density varied between the different readers used and so the duration of the initial signal summation was adjusted to include the initial ~50% of the signal decay). The background subtracted from the initial signal was based on the subsequent ~0.3 s of stimulation. Multi-grain aliquots were mounted in stainless steel cups using an ~5 mm spot of silicone oil; each aliquot contained approximately 800 individual grains (Duller, 2008b).

3.3.2. Cobble OSL measurements

The OSL measurements of the quartz extracted from the cobbles made use of a preheat of 190 °C (held for 10 s), a cutheat of 150 °C and a test dose of 65 Gy unless otherwise stated. The signal was summed over the initial 0.8 s of stimulation, background corrected using the subsequent 0.8 s of stimulation. Multi-grain aliquots were mounted on stainless steel discs coated with silicone oil (8 mm), i.e.each aliquot contained approximately 1100 grains (Duller, 2008b).

4. Dosimetry

This section describes the measured dose rates and the corrections for heterogeneity in the radiation field for both sediment samples and cobbles. For the sediments, we consider the proximity to bedrock, whereas for the cobbles we only need to consider the surrounding sediment as the nearest bedrock was >30 cm away.

Table 2
Radionuclide concentrations and infinite matrix dose rates for quartz extracted from sediment (TA2247-61) and cobble (TA2265-68) samples. The data for the cobbles are reproduced from Thomsen et al. (2016). Sample TA2262 is taken from bedrock. For sediment samples, a 20 ± 10% escape of ^{222}Rn is assumed in dose rate calculations.

Sample	Depth (cm)	Unit	Radionuclide concentrations (Bq kg^{-1})				Infinite matrix dry dose rates (Gy ka^{-1})	
			^{238}U	^{226}Ra	^{232}Th	^{40}K	Gamma	Beta
TA2247	221	B	7 ± 4	7.3 ± 0.4	14.3 ± 0.4	110 ± 6	0.31 ± 0.01	0.45 ± 0.02
TA2249	213	C	16 ± 5	14.3 ± 0.4	29.3 ± 0.5	161 ± 7	0.57 ± 0.01	0.75 ± 0.02
TA2248	205	C	13 ± 4	17.7 ± 0.4	24.1 ± 0.4	146 ± 6	0.52 ± 0.02	0.71 ± 0.02
TA2250	197	C	14 ± 1	19.3 ± 0.2	28.9 ± 0.2	142 ± 2	0.59 ± 0.02	0.75 ± 0.02
TA2251	181	C	10 ± 2	15.8 ± 0.2	24.6 ± 0.2	246 ± 4	0.59 ± 0.01	0.94 ± 0.01
TA2252	168	C/D	19 ± 2	24.6 ± 0.3	30.4 ± 0.3	423 ± 5	0.86 ± 0.02	1.52 ± 0.02
TA2253	160	D1	10 ± 5	21.5 ± 0.8	26.6 ± 0.9	444 ± 14	0.81 ± 0.02	1.52 ± 0.04
TA2255	159	D1	15 ± 4	20.2 ± 0.4	24.4 ± 0.4	469 ± 9	0.80 ± 0.02	1.55 ± 0.03
TA2254	154	D1	25 ± 5	23.0 ± 0.5	27.0 ± 0.5	525 ± 11	0.89 ± 0.02	1.74 ± 0.03
TA2256	153	D1	15 ± 10	22.7 ± 0.8	28.9 ± 0.9	532 ± 15	0.92 ± 0.03	1.77 ± 0.04
TA2257	138	D2	27 ± 2	29.0 ± 0.4	34.5 ± 0.3	508 ± 5	1.01 ± 0.02	1.81 ± 0.03
TA2258	127	D3	17 ± 2	23.0 ± 0.3	25.0 ± 0.2	686 ± 6	1.00 ± 0.02	2.13 ± 0.02
TA2259	122	D3	17 ± 4	26.7 ± 0.4	31.0 ± 0.4	664 ± 10	1.07 ± 0.02	2.15 ± 0.03
TA2260	115	D3	16 ± 6	28.5 ± 0.6	32.9 ± 0.7	567 ± 13	1.03 ± 0.02	1.94 ± 0.04
TA2261	108	D3	18 ± 2	24.0 ± 0.2	27.4 ± 0.2	632 ± 5	0.99 ± 0.02	2.02 ± 0.02
TA2262	–	–	17 ± 17	19.3 ± 1.1	4.9 ± 1.0	30 ± 14	0.22 ± 0.02	0.30 ± 0.04
TA2265	154	D1	−2 ± 4	5.8 ± 1.0	7.2 ± 1.0	60 ± 12	0.17 ± 0.02	0.26 ± 0.03
TA2266	138	D2	17 ± 17	10.3 ± 1.1	4.9 ± 1.0	30 ± 14	0.15 ± 0.02	0.21 ± 0.04
TA2267	138	D2	−2 ± 13	6.2 ± 0.9	8.9 ± 0.9	48 ± 10	0.19 ± 0.02	0.24 ± 0.03
TA2268	138	D2	19 ± 11	15.9 ± 0.8	6.6 ± 0.7	66 ± 9	0.24 ± 0.02	0.37 ± 0.02

4.1. Infinite matrix dose rates

The radionuclide concentrations and dry infinite matrix dose rates, assuming a mean grain size of 180 μm and 215 μm for quartz extracted from cobbles and sediments, respectively, are summarised in Table 2. The dry infinite matrix beta and gamma dose rates are also given, derived assuming a 20±10% loss of ^{222}Rn compared to its parent ^{226}Ra. Total dose rates to the surface slices are shown in Table 4 and total dose rate to the depths later argued to be well-bleached are summarised in Table 5.

In contrast to ^{226}Ra, concentrations of the series parent ^{238}U are poorly known, but on average, the activity ratio ^{226}Ra/^{238}U in the sediments is 1.36±0.08 (n=15). This suggests there may be a small excess of ^{226}Ra. In such a carbonate-rich environment, this is most likely due to ^{238}U mobilisation, leaving behind ^{230}Th ($\tau_{1/2}$ ~75 ka) and progeny, and so should have a negligible effect on the time-averaged total dose rate. The radionuclide concentration ratios of the sediment to rock samples are, on average 3.3±0.4 (n=4 nuclides; weighted by the uncertainties on the individual ratios). The activity concentrations in the sediments decrease systematically with decreasing elevation (Fig. 2), and as a result, there is a significant change in dose rate with sediment depth. If we assume that the sediments have been derived primarily from the surrounding host rock, and that radionuclides (especially Th) behave conservatively, this increase in radionuclide concentration implies a loss of some 75% of non-radioactive carbonate by dissolution. If this process happened after deposition, then it presumably occurred after sedimentation was complete (because the youngest sediments have been modified most). Alternatively, and in our opinion more likely, this enrichment took place before deposition and the systematic change in concentrations with elevation arise from grain-size selection in the transport/deposition process changing with elevation. The second assumption is employed in age calculations, i.e. the measured radionuclide concentrations are assumed to have persisted throughout the life of the site. For the sediment samples, the dry beta dose rates vary between ~ 2 Gy ka^{-1} and ~ 0.5 Gy ka^{-1}, and the corresponding dry gamma dose rates vary between ~ 1 Gy ka^{-1} and ~ 0.3 Gy ka^{-1}. The total infinite-matrix dose rates vary from ~ 3 Gy ka^{-1} at the top of the sequence (sample TA2261) to ~ 0.8 Gy ka^{-1} at the bottom (sample TA2247); see Fig. 2 and Fig. 2. The bedrock sample has a dry gamma dose rate of ~ 0.2 Gy ka^{-1}. Thus, for all samples except the deepest (TA2247) the dry gamma dose rate is more than two times larger for the sediments than for the bedrock sample. As some of the sediment samples are taken within 15 cm of the bedrock, the dose rates to all sediment samples have been modified to take into account the heterogeneity in the gamma field arising due to the proximity to bedrock (see Fig. 1). This modelling is described in Section 4.2.1.

The infinite matrix dry dose rates for the four cobbles are similar to each other and to the bedrock sample (TA2262) with averages of 0.28±0.03 Gy ka^{-1} and 0.19±0.02 Gy ka^{-1} for beta and gamma dose rates, respectively. However, dose rate modelling for the cobbles is necessary to account for the beta dose rate gradient at the rock-to-surface interface, as the total beta dose rate varies with depth due to contribution from i) the surrounding sediments and (ii) from the rock sample itself (see Section 4.2.2 for details).

4.2. Dose rate modelling

In environments where the infinite matrix dose rate assumption (Aitken, 1985; Guérin et al., 2012) is not fulfilled, e.g.in a heterogeneous sample matrix, accurate estimation of the field dose rate in the medium of interest requires modifications to the infinite matrix dose rate for the sample. In this study, some of the sediment samples were taken relatively close (i.e.<30 cm) to bedrock or the collapsed shelter roof (see Table 1) and given that the gamma dose rate for bedrock is between ~1.5 and 5 times lower than that from the sediment, the gamma radiation field in the vicinity of at least these samples must have a gradient, which will have an impact on the dose rate experienced by the sediment samples. For the cobbles, one should in addition also consider the variation of dose rate with depth into the rock.

A simple correction model to deal with such issues was developed and is described in details in Freiesleben (2021). This model relies on the principle of superposition and corrects the infinite matrix dose rate to take into account the finite size of the sample (see Eq. (2) below). The model also corrects for the dose rate from the surrounding material on one or more sides (see Eq. (3) below). The model is cubic such that only 6 distances are required, from the point of interest to the nearest material interface (front, back, left, right, top, bottom).

The total effective external radionuclide dose rate at a given position (X, Y, Z coordinates) is the sum of the total beta (β) and gamma (γ) contributions $\dot{D}_{\mathrm{total},i}$, with i being β or γ. (As the outer ~ 10 μm of the grains are etched away by the hydrofluoric acid treatment, any contribution from alpha radiation is negligible and is ignored here).

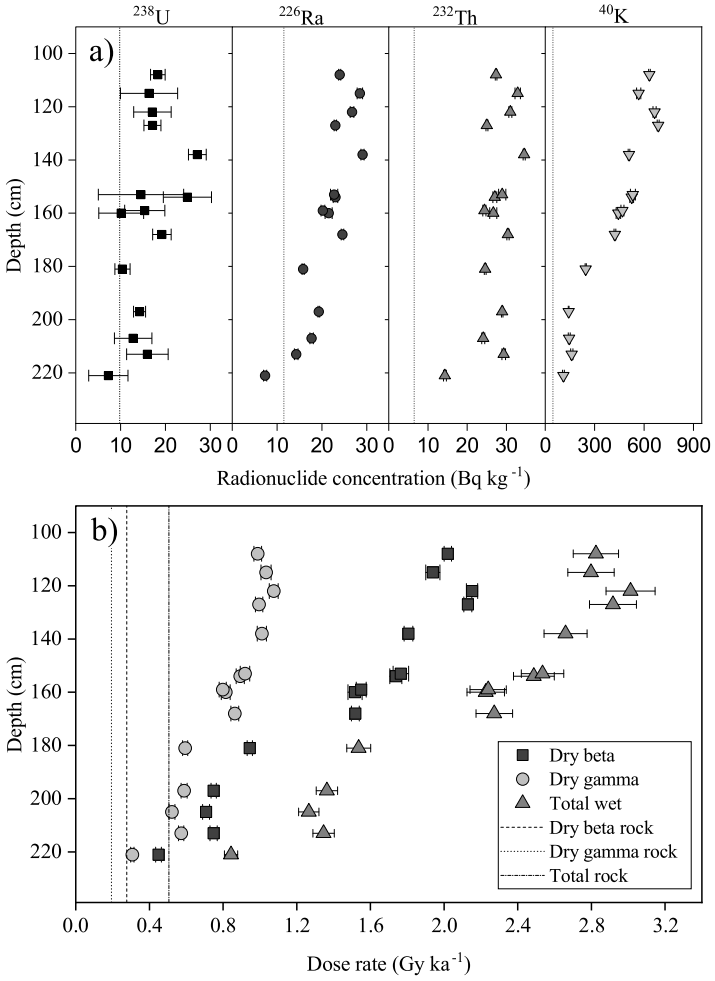

Fig. 2. Dosimetric data for the sediments as a function of depth. Also shown are average values for bedrock/cobbles (vertical lines). (a) Radionuclide concentrations and (b) Dry beta, dry gamma and total wet sediment dose rates.

Each $\dot{D}_{\text{total},i}$ changes with depth due to dose rate attenuation effects in the material in question (here rock or sediment). Each $\dot{D}_{\text{total},i}$ can be expressed as the sum of contributions from the infinite matrix dose rate originating from the surrounding medium ($\dot{D}_{\text{sur,inf}}$) and from the medium itself ($\dot{D}_{\text{med,inf}}$), i.e.

$$\dot{D}_{\text{total}} = C_{\text{med}}\dot{D}_{\text{med,inf}} + C_{\text{sur}}\dot{D}_{\text{sur,inf}} \quad (1)$$

for each of the two radiation types included here. Because of attenuation effects, the infinite matrix dose rate terms need to be modified using the correction factors C_{med} and C_{sur}, which are given as

$$C_{\text{med}} = (1 - X_{m,m})(1 - Y_{m,m})(1 - Z_{m,m}) \quad (2)$$

$$C_{\text{sur}} = X_{m,s} + (1 - X_{s,s})Y_{m,s} + (1 - X_{s,s})(1 - Y_{s,s})Z_{m,s} \quad (3)$$

$$X_{m,m} = f_{m1}e^{-c_{m1}x_1} + f_{m2}e^{-c_{m2}x_2} \quad (4)$$

$$X_{m,s} = f_{s1}e^{-c_{m1}x_1} + f_{s2}e^{-c_{m2}x_2} \quad (5)$$

where f_{m1}, f_{m2}, f_{s1} and f_{s2} are the fractional dose rate factors for the sample material m and the surrounding material s, respectively. c_{m1} and c_{m2} are the linear attenuation coefficients in material m, where x_1 and x_2 are the distances from the point of interest to the boundary between the medium and the surrounding material in the xth-direction. f_{m1}, f_{m2}, c_{m1} and c_{m2} depend on the radiation type, on the type of material and on the distances in the xth-direction (i.e. x_1 and x_2). Similar relationships (Eqs. (4) and (5)) apply to the y- and z-directions, i.e.$Y_{m,m}$ and $Z_{m,m}$, and $Y_{m,s}$ and $Z_{m,s}$, respectively.

Eq. (1) gives the dry beta or gamma external dose rate and thus must also be corrected for water content. This simple approximation to correction for heterogeneity in the dose rate field can be applied to both rocks surrounded by sediment (in this case, the rock will have the subscript m and the sediment s) and to sediment samples positioned close to bedrock (in this case, the rock will have the subscript s and the sediment m). In this study, we have assumed that the cobbles can be approximated by cubes with dimensions length=height=width=h (the thickness of the cobble).

Finally, dose rates due to cosmic radiation (not significantly dependent on depth into the rock over the scales considered here) and contributions arising from internal uranium and thorium activity (giving rise to an internal dose rate) are added to give the total dose rate, modified for the effect of grain size attenuation. In the cobbles, the dose rate changes significantly with depth into the rock and thus must be calculated for individual depths. The dose rate in interval x_i to x_f, was estimated from numerical integration of the depth dependent dose rate over the depth of the slice.

The cobble material at this site is limestone and the linear attenuation values (c) can be approximated by the corresponding linear attenuation values for sediment (Riedesel and Autzen, 2020) corrected to a density of 2 g cm^{-3}. The values used are summarised in Table 3.

Table 3
Beta and gamma attenuation factors (c) and fractional dose factors (f) for different distances (d) in limestone (with a density of 2 g cm^{-3}) to the boundary between the limestone and the surrounding sediment. Adapted from Riedesel and Autzen (2020) after density correction.

	Beta			Gamma		
Decay chain	c (mm^{-1})	f	d (mm)	c (mm^{-1})	f	d (mm)
^{40}K	2.81	0.50	all	0.0215	0.50	<10
				0.0138	0.45	>10
^{232}Th	4.66	0.50	<0.15	0.020	0.50	<10
	1.84	0.34	>0.15	0.0138	0.42	>10
^{238}U	3.52	0.50	<0.15	0.0277	0.50	<10
	1.5	0.37	>0.15	0.0154	0.45	>10

The attenuation coefficients c used for the sediments (data not shown) are 10% lower than those given in Table 3, since the density for the sediments is taken as 1.8 g cm^{-3}.

In the following, we investigate the effect on the dose rate when applying this dose rate modelling approach to our data.

4.2.1. Sand-sized sediment dose rate modelling

Fig. 3 shows an example of how the dose rate (gamma, beta and the sum of the two) varies in sediment (light red area) surrounded by bedrock and the collapsed shelter roof (both represented by the grey area). Here we have assumed that the total vertical distance between the bedrock and the shelter roof is 85 cm. In addition, we assume that the horizontal distance to bedrock is 42 cm on one side and infinite on the other. In the last direction (i.e.perpendicular to the section) we also assume that the distance to bedrock/shelter roof is infinite. Here, we have used the dose rate data from samples TA2254 (sediment) and TA2262 (bedrock). As expected the beta dose rate is essentially constant as a function of vertical distance (except for the first 1.5 mm), whereas the gamma contribution increases by 13% over the first ~ 15 cm from bedrock where after it remains constant, i.e.only when the sediment sample is taken within ~ 15 cm of bedrock/shelter roof is there a significant change in the dose rate compared to the infinite matrix dose rate. Sample TA2254 is located 25 cm above bedrock and 60 cm below the collapsed shelter roof (see Table 1 and the diamond symbol in Fig. 3) and the total dose rate correction to the infinite matrix dose rate is thus ~ 1%.

The average correction factor for the gamma dose rate to the sediment samples due to the proximity to bedrock is 0.954±0.007 (n=15) (i.e.a 4.6% decrease) leading to a small correction factor for the total dose rate of 0.983±0.003 on average (1.7% decrease), with the largest correction factor of 0.967±0.06 (3.3% decrease) for sample TA2251. The dose rates used for age calculation are given in Table 4 as "$\dot{D}_{tot}$". These are based on measured beta and corrected gamma dose rates, both adjusted for water content and grain size attenuation, and including internal dose rates and the cosmic ray contribution (~ 10% of the total).

4.2.2. Cobble dose rate modelling

Fig. 4 shows the beta, gamma and total dose rate at different sample positions in the x-direction for cobble TA2265. The dose rate used for the surrounding sediment is that of sample TA2254, which was taken in close proximity to the cobble. As expected the gamma dose rate remains constant within the cobble (unaffected by the sediment/cobble boundary), whereas the beta dose rate drops rapidly at the boundary. However, it is only to a depth of ~ 2 mm (corresponding to the first two slices) that there is a significant depth dependence. The dose rate in the first slice differs from that in the centre by ~20%, whereas the second slice only differs by 1% from the centre. Note that near the surface, the dose rate decreases with depth because the dose rate in the cobbles compared is significantly smaller than the dose rate from the surrounding sediment. If the dose rate for the cobbles had been significantly larger than for the surrounding sediment, one would expect the dose rate to increase with depth in the first ~ 2 mm.

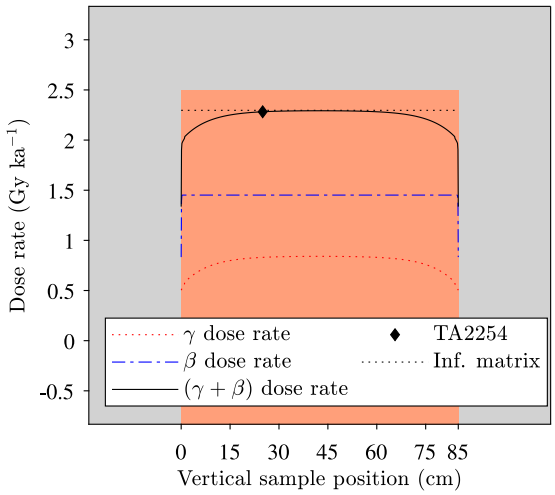

Fig. 3. Modelled dose rates in sediment (light red area in the centre) surrounded by rock material (grey area) as a function of vertical sample position within the sediment. Vertically the sediment is sandwiched in between bedrock (x=0 cm) and the collapsed shelter roof (x=85 cm). The horizontal distance to bedrock on one side is in the model assumed to be infinite and on the other side 42 cm. This is illustrated by drawing the sediment with a finite horizontal distance in one direction (upwards on the plot) and non-finite in the other (downwards on the plot). The distance to nearby bed rock in the last direction (i.e.the z-direction) is non-finite (not shown in the figure). Beta (β, dashed–dotted blue line), gamma without cosmic (γ, dotted red line) and the total (solid black line) dose rates are shown (i.e.the cosmic contribution and other internal contributions have not been included). Similarly, the infinite matrix dose rate in the sediment is shown with a dashed black line. The dose rate data for sample TA2254 (sediment) and TA2262 (bedrock) have been used. The actual position of sample TA2254 is indicated on the total dose rate (without cosmic) curve with a diamond symbol.

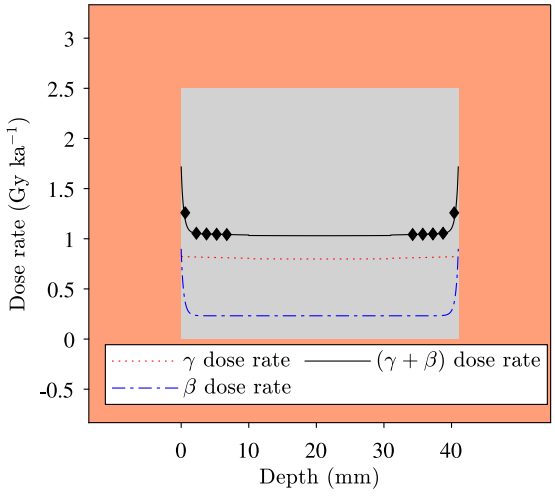

Fig. 4. Modelled dose rates in cobble TA2265 (grey area, dimensions 41 × 1201u x120 mm) surrounded by sediment (light red area; assumed non-finite in all directions) as a function of depth into the cobble. Beta (β, dashed–dotted blue line), gamma without cosmic (γ, dotted red line), and the total (solid black line) dose rates at different depths in cobble TA2265. The sediment infinite matrix dose rate used is that measured for sediment sample TA2254 and it has been corrected for water content and beta attenuation. Black diamond symbols indicate the depths of the first 5 slices in cobble TA2265.

5. OSL results

5.1. Luminescence characteristics

5.1.1. Sand-sized sediment quartz luminescence characteristics

The inset to Fig. 5a shows that the OSL stimulation curve is similar to that derived from Risø calibration quartz, which is known to

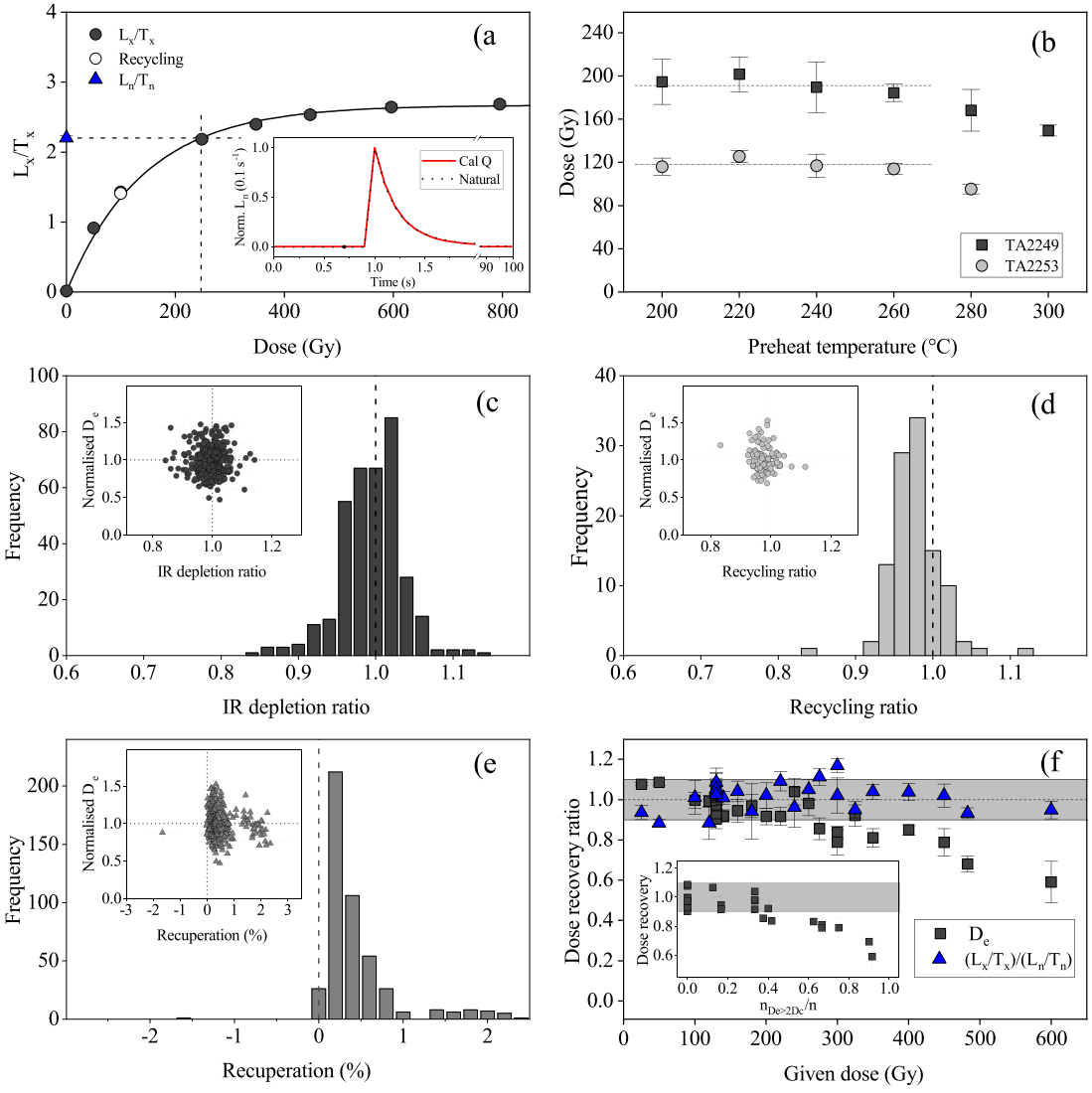

Fig. 5. Sand-sized quartz from sediment: luminescence characteristics. (a) Representative dose response curve from sediment sample TA2253. Filled circles: regenerated points. Open circle: recycling point at 100 Gy. Triangle: natural sensitivity corrected signal. The data are taken from a dose recovery experiment with a given dose of 350 Gy, and have been fitted using a saturating exponential function ($y = A \times [1 - exp(-x/D_c)]$). The inset shows the normalised OSL stimulation curve of the natural signal (dashed line) and that from calibration quartz (solid line), which is known to be fast-component dominated. Note that detection started 1 s prior to the optical stimulation. (b) Natural preheat plateau for samples TA2249 and TA2253. The cutheat temperature was 40 °C less than the preheat temperature. Individual points are an average of doses obtained for at least 3 aliquots measured at each preheat temperature. Also shown as horizontal lines are the average doses for preheat temperatures ranging between 200 and 260 °C. (c) Frequency histogram of measured IR depletion ratios for all sediment samples. The vertical dashed line indicates an IR depletion value of unity. Inset shows individual aliquot D_e values (normalised to average D_e of each sample) as a function of IR depletion ratio. Dashed horizontal and vertical lines indicate unity values. (d) same as (c) but for the recycling ratio. (e) same as (d) but for the relative recuperation (i.e.the ratio of the sensitivity corrected recuperated signal to the sensitivity corrected natural signal). Here the vertical lines indicate a value of zero. (f) Dose recovery results for given doses ranging between 25 and 600 Gy using a test dose of 50 Gy (n>6). Squares (D_e) indicate dose recovery ratios calculated by taking the arithmetic mean of the individual measured doses. Triangles indicate light recovery ratios, i.e.the ratio of the sensitivity corrected signal from a regenerated dose (L_x/T_x, equal to the given dose) to that from the given dose (L_n/T_n). The inset shows the dependence of the dose recovery ratio on the relative number of aliquots with dose estimates larger than $2 \times D_c$ (including aliquots not giving bounded dose estimates).

be fast-component dominated (Hansen et al., 2015). This comparison shows that the OSL signals from the sediment quartz samples are fast-component dominated and any contributions from isothermal TL signals are negligible. Equivalent dose estimation is based on a SAR protocol employing a minimum of three sensitivity corrected regeneration points (L_x/T_x), a recuperation point and a recycling point and in most cases also an IR depletion point. Fig. 5a shows a representative dose response curve (DRC) from sample TA2253 measured using a preheat of 260 °C and a cutheat of 220 °C. As with the other samples from this site, we are able to accurately repeat the response to a given regeneration dose (the recycling point, open symbol), the build-up of signal between SAR cycles (recuperation) is negligible and the laboratory DRC is well-represented by a single saturating exponential function. The average sensitivity change (here defined as the last regeneration test dose divided by the first (natural) test dose), IR depletion ratio, recycling ratio and recuperation value (taken relative to the natural signal) for aliquots included in the dose estimation are 2.63 ± 0.10 (n=466), 0.994 ± 0.002 (n=358), 0.973 ± 0.002 (n=466) and $0.44 \pm 0.02\%$ (n=466), respectively. Thus, the chosen SAR protocol reproducibly measures the luminescence response to a laboratory dose, despite the significant sensitivity change. The average D_c value for DRCs measured with a test dose of 50 Gy and a largest regeneration dose of 300 Gy is 122 ± 3 Gy (n=302).

Fig. 5b shows the average equivalent dose measured for sample TA2249 and TA2253 as a function of preheat temperature. The estimated dose is independent of the preheat temperature in the interval

Table 4
Summary of sediment and cobble surface data. TA2247-61 are sediment samples, whereas TA2265-68 are Cobbles. "t" and "b" after the cobble name indicates "top" and "bottom", respectively. The cobble data reported in this Table are from surface slices only (i.e.depths < 1.2 mm). Full luminescence-depth profiles have not been measured and thus no claims regarding the completeness of bleaching at deposition can be made for these data. "GFU" is the geoarchaeological unit described in Aubry et al. (2014), "D_e" is the arithmetic equivalent dose (after application of the IQR criterion), "n_a" is the number of accepted aliquots, "n_r" is the total number of rejected aliquots, i.e.both unbounded dose estimates and outliers (IQR), "n_{sat}" is the number of aliquots not giving a bounded dose estimate, "Sat" is the relative number of aliquots not giving a bounded dose estimate relative to the total number of measured aliquots, "$\dot{D}_{tot}$" is the total dose rate after correction for gamma heterogeneity, and "OSL age" is $D_e/\dot{D}_{tot}$. The equivalent dose (and thus OSL age) for sample TA2247 is regarded as a minimum age due to saturation issues (see text for details).

Sample	GFU	Depth (cm)	D_e (Gy)			n_a	n_r	n_{sat}	sat. (%)	$\dot{D}_{tot}$ (Gy ka^{-1})			Age (ka)		
TA2247	B	221	310	±	27	9	14	14	61	0.83	±	0.04	>	370	
TA2249	C	213	184	±	8	42	1	1	2	1.32	±	0.06	140	±	9
TA2248	C	205	118	±	2	53	8	1	2	1.23	±	0.05	96	±	5
TA2250	C	197	126	±	4	22	3	1	4	1.34	±	0.06	94	±	5
TA2251	C	181	159	±	5	19	6	2	8	1.49	±	0.06	107	±	6
TA2252	C/D	168	119	±	3	30	1	0	0	2.21	±	0.10	54	±	3
TA2253	D1	160	114	±	4	20	2	0	0	2.21	±	0.10	52	±	3
TA2255	D1	159	117	±	3	30	3	1	3	2.18	±	0.10	53	±	3
TA2254	D1	154	125	±	3	37	2	1	3	2.48	±	0.11	51	±	3
TA2256	D1	153	125	±	4	23	4	1	4	2.49	±	0.11	50	±	3
TA2257	D2	138	121	±	3	54	6	1	2	2.63	±	0.12	46	±	2
TA2258	D3	127	121	±	4	32	3	2	6	2.91	±	0.13	41	±	2
TA2259	D3	122	113	±	3	28	7	3	9	3.00	±	0.13	37	±	2
TA2260	D3	115	115	±	4	30	1	0	0	2.78	±	0.12	41	±	2
TA2261	D3	108	115	±	4	28	2	2	6	2.78	±	0.12	41	±	2
TA2265t	D2	138	104	±	6	49	0	0	0	1.43	±	0.04	72	±	5
TA2265b	D2	138	75	±	4	54	1	0	0	1.43	±	0.04	52	±	3
TA2266t	D2	138	132	±	12	47	3	0	0	1.64	±	0.03	80	±	8
TA2266b	D2	138	80	±	5	39	1	0	0	1.64	±	0.03	48	±	3
TA2267b	D2	138	94	±	7	29	1	0	0	1.43	±	0.04	65	±	5
TA2268t	D1	154	85	±	5	52	5	0	0	1.43	±	0.04	59	±	4
TA2268b	D1	154	95	±	5	55	1	0	0	1.43	±	0.04	66	±	4

Table 5
Summary of cobble results from the individual slices identified to be well-bleached by the ratio of the present-day profile to the predicted pre-burial profile. Equivalent doses (De), total dose rate ($\dot{D}_{tot}$), and average OSL ages (Age_{wb}) from the individual slices are given. n is total number of aliquots for each depth. $Age_{wb,t}$ and $Age_{wb,b}$ are averaged OSL ages for the top and bottom of the individual cobbles, respectively, after applying the IQR rejection criteria. n_a is the number of accepted aliquots after applying the IQR rejection criterion. Note that no $Age_{wb,t}$ is given for TA2267 as the cobble was too fragile to obtain a full length core. Age uncertainties include both random and systematic uncertainties.

Sample	Side	Depth (mm)	D_e (Gy)	n	$\dot{D}_{tot}$ (Gy ka^{-1})	Age_{wb} (ka)	$Age_{wb,t}$ (ka)	$Age_{wb,b}$ (ka)	n_a
TA2265_2	Top	0.6	64 ± 6	6	1.45 ± 0.04	44 ± 5	50±4		21
TA2265_2	Top	2.25	64 ± 6	3	1.24 ± 0.04	51 ± 5			
TA2265_3	Top	0.6	79 ± 12	4	1.45 ± 0.04	55 ± 8			
TA2265_3	Top	2.25	67 ± 11	3	1.24 ± 0.04	54 ± 9			
TA2265_1	Bottom	40.4	69 ± 10	7	1.45 ± 0.04	47 ± 7		50 ± 5	23
TA2265_2	Bottom	40.4	104 ± 21	4	1.45 ± 0.04	72 ± 14			
TA2265_3	Bottom	40.4	65 ± 8	12	1.45 ± 0.04	45 ± 6			
TA2266	Top	0.6	55 ± 8	8	1.53 ± 0.04	36 ± 5	33±2		15
TA2266	Top	2.25	54 ± 9	6	1.31 ± 0.04	41 ± 7			
TA2266	Top	3.75	43 ± 3	3	1.30 ± 0.04	33 ± 3			
TA2266	Bottom	34.75	105 ± 34	3	1.30 ± 0.04	81 ± 27		62±12	12
TA2266	Bottom	36.25	26 ± 25	2	1.30 ± 0.04	20 ± 19			
TA2266	Bottom	37.75	48 ± 22	3	1.31 ± 0.04	37 ± 17			
TA2266	Bottom	39.4	135 ± 20	4	1.53 ± 0.04	88 ± 13			
TA2267	Bottom	44.75	84 ± 19	5	1.32 ± 0.04	64 ± 13	–	56±4	13
TA2267	Bottom	46.25	81 ± 3	3	1.32 ± 0.04	61 ± 3			
TA2267	Bottom	47.75	82 ± 8	3	1.33 ± 0.04	62 ± 6			
TA2267	Bottom	49.55	79 ± 10	3	1.55 ± 0.03	51 ± 7			
TA2268_2	Top	0.6	138 ± 28	3	1.66 ± 0.03	83 ± 17	74±7		18
TA2268_2	Top	2.25	87 ± 12	3	1.46 ± 0.03	60 ± 9			
TA2268_2	Top	3.75	111 ± 6	3	1.45 ± 0.03	76 ± 5			
TA2268_2	Top	5.25	135 ± 16	3	1.45 ± 0.03	93 ± 12			
TA2268_3	Top	0.6	143 ± 44	3	1.66 ± 0.03	87 ± 27			
TA2268_3	Top	2.25	63 ± 10	3	1.46 ± 0.03	44 ± 7			
TA2268_1	Bottom	41.4	42 ± 7	5	1.66 ± 0.03	25 ± 4		43±4	18
TA2268_2	Bottom	39.75	73 ± 11	3	1.46 ± 0.03	50 ± 7			
TA2268_2	Bottom	41.4	99 ± 14	8	1.66 ± 0.03	60 ± 8			
TA2268_3	Bottom	41.4	71 ± 11	3	1.66 ± 0.03	43 ± 7			

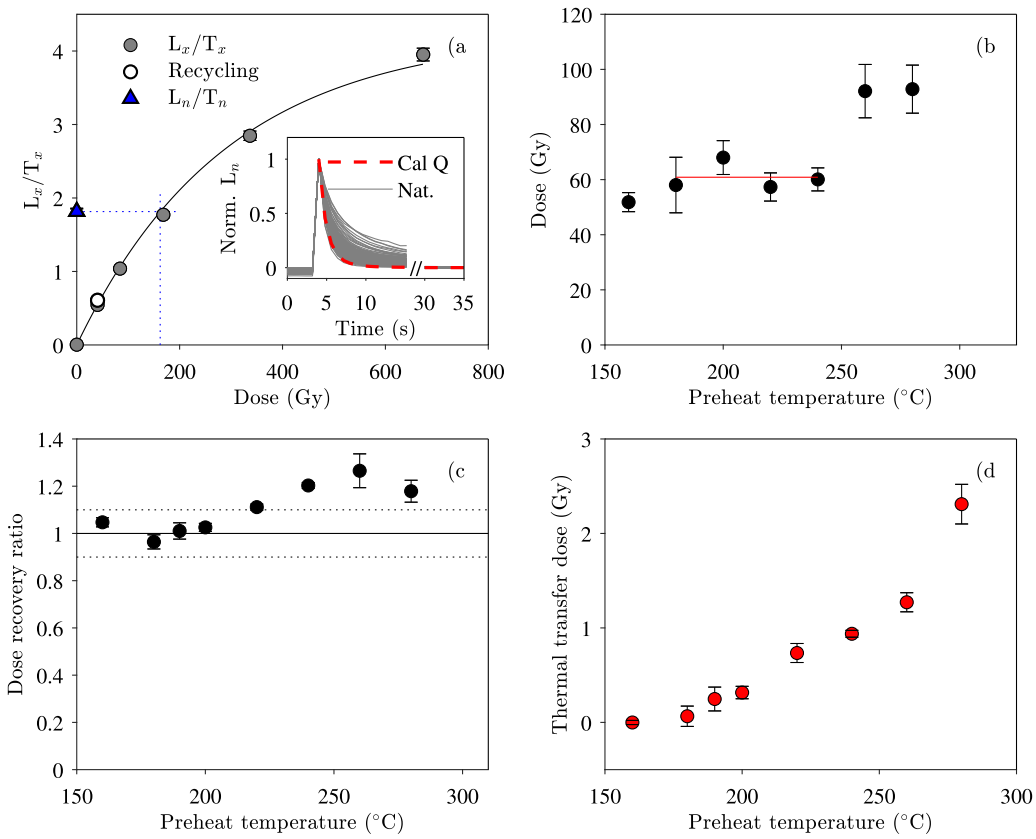

Fig. 6. (a) Typical dose response curve from a surface slice from cobble TA2268. Circles: sensitivity corrected regenerated OSL signals. Triangle: natural sensitivity corrected OSL signal (L_n/T_n). Open circle: recycling point. Inset in (a) Range of OSL stimulation curves measured for the natural signal (grey solid lines). For comparison, the natural stimulation curve measured from an aliquot of calibration quartz is also shown (dashed red line). (b) Surface natural doses dependence on preheat temperature using three aliquots for each preheat temperature for surface slices from cobble TA2268. The red horizontal line indicates the thermally stable plateau. (c) The ratio of the measured doses (after correction for thermal transfer) to the known given dose of 67 Gy (dose recovery ratio). (d) Thermal transfer (T) doses used to for correction in the dose recovery experiment.

200 to 260 °C. Above this interval the equivalent dose appears to decrease.

Figs. 5c, 5d and 5e show frequency histograms of individual IR depletion ratios, recycling ratios and relative recuperation values, respectively. The respective insets show the relationship between these values and their individual dose estimates (normalised to the sample average). Clearly, there is no correlation with dose and applying commonly used rejection criteria (e.g.recycling ratios must be consistent with unity within two standard deviations) would only result in less precise dose estimates (see Murray et al., 2021, and references therein).

To evaluate our ability to recover a known given dose using the chosen measurement protocol, a series of dose recovery experiments were undertaken. In these experiments, the individual aliquots were first bleached twice for 100 s (with an intervening pause of 10,000 s) using the blue LEDs at room temperature, before a laboratory dose ranging between 25 and 600 Gy was given to individual aliquots. Our chosen SAR protocol was then used to measure these laboratory given doses. Dose recovery ratios (measured dose divided by given dose) are shown as a function of given dose in Fig. 5f (squares), where each point is an average of doses determined from at least 6 individual aliquots. All dose recovery ratios up to a given dose of 260 Gy (corresponding to $\sim 2.1 \times D_c$) are considered to be satisfactory (i.e.within ±10% of unity), but for larger given doses the dose recovery ratio decreases with given dose. The inset to Fig. 5f shows how the dose recovery ratio varies as a function of the relative number of individual dose estimates which interpolate above $2 \times D_c$ on the dose response curve (or do not interpolate on the dose response curve at all, i.e.no bounded dose estimate could be derived). When the number of individual aliquots with $D_e > 2 \times D_c$ is $\gtrsim$40% the dose recovery ratio becomes unacceptable, i.e.< 0.9. Thus, our ability to recover a laboratory dose decreases as the number of aliquots interpolating above $2 \times D_c$ increases. However, as pointed out by Murray et al. (2021), the sensitivity-corrected luminescence (L_n/T_n) is the measured quantity, not the dose. In the saturating part of the dose response curve even small uncertainties in this (L_n/T_n) ratio will be greatly enhanced on the dose axis and can thus lead to unbounded estimates of dose; these cannot be included in the dose recovery ratio, which is thus biased towards those values which can be interpolated, i.e. low values. Rather, in order to determine whether the protocol is performing as well as can be expected, one should investigate the behaviour of the light recovery ratio, i.e.the ratio of the sensitivity corrected signal from a regenerated dose (L_x/T_x, equal to the given dose) to the signal from the given dose (L_n/T_n). This ratio does not involve interpolation, and so includes values greater than unity. This average ratio of the sensitivity corrected light levels is also shown in Fig. 5f, and indeed the values are acceptable for all given doses. Thus, the light levels can be accurately recovered up to at least 600 Gy, and so the underestimation observed in the dose recovery ratios for given doses larger than approximately 260 Gy is not caused by the luminescence characteristics. Rather it arises from the bias involved in interpolation on the DRC and the unavoidable rejection of non-finite dose estimates (Singh et al., 2017).

5.1.2. *Cobble quartz luminescence characteristics*

A single-aliquot regenerative (SAR) protocol (Wintle and Murray, 2006) was adopted for equivalent-dose measurements (see Section 3.3). Fig. 6a shows a SAR dose response curve from a surface slice of cobble TA2268 and the inset shows representative natural OSL decay curves (grey lines). A significant difference in decay shapes is observed with variable amounts of medium component. For comparison a calibration quartz decay curve (dashed red line) is also shown. Despite a variable

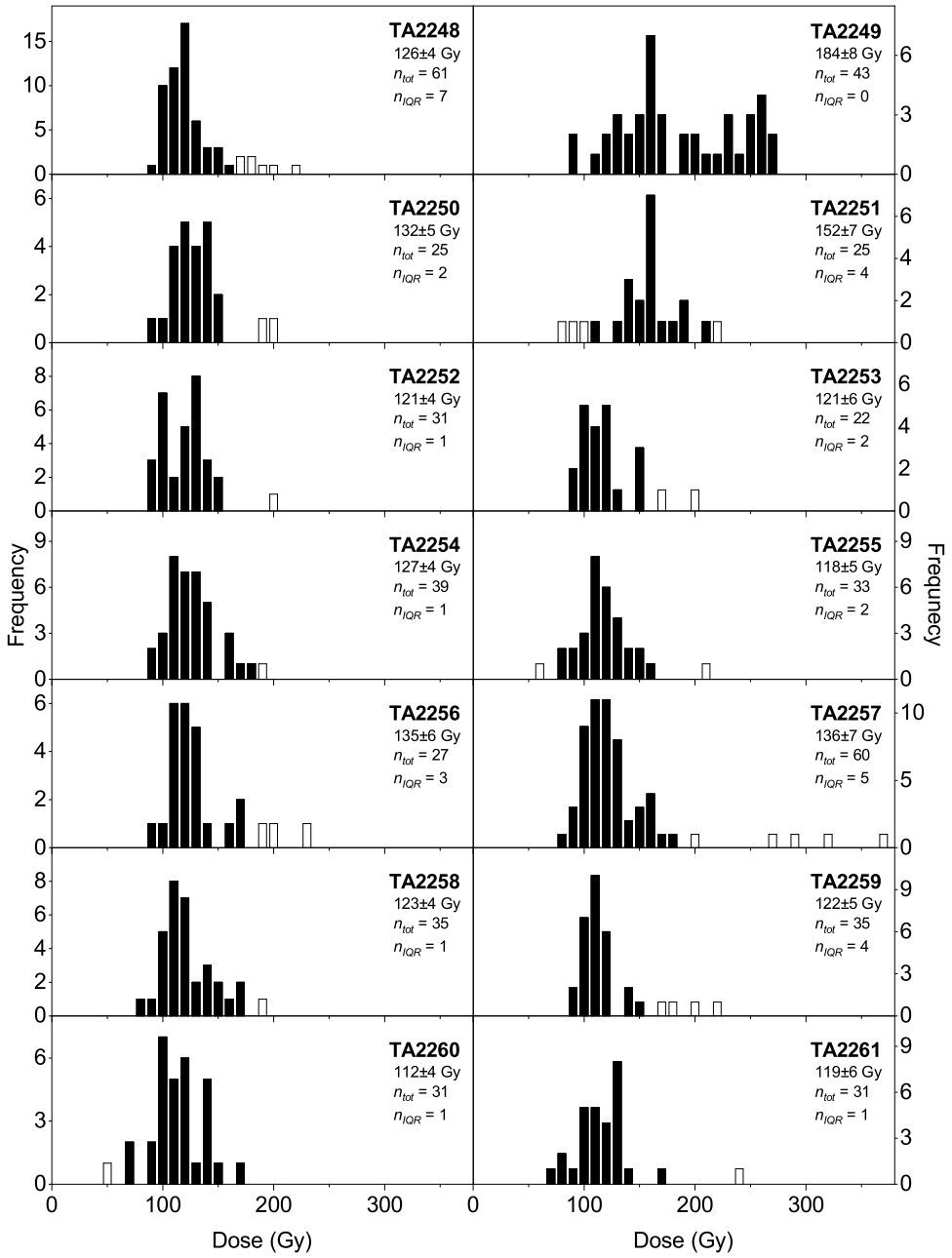

Fig. 7. Sediment multi-grain dose distributions for all samples, except sample TA2247 for which only 9 aliquots gave bounded dose estimates, i.e.61% of the measured L_n/T_n values did not give bounded dose estimates when interpolating onto the respective dose response curves. Doses accepted after application of the IQR criterion are shown as black bars, whereas rejected dose estimates are shown as white bars. The legend for each sample gives the arithmetic mean dose and its standard error of all measured aliquots giving a bounded dose estimate. Also given is the total number of measured aliquots (n_{tot}) and the number of aliquots rejected by the IQR criterion (n_{IQR}).

contribution from medium/slow components, on average the natural OSL signal is dominated by the fast-component. The use of early background subtraction helps to maximise the fast component contribution in signal summation (Ballarini et al., 2007; Murray et al., 2021).

In order to determine the appropriate measurement conditions, natural and dose recovery preheat tests were carried out using quartz grains extracted from the surface slices taken from cobble sample TA2268 (see Fig. 6b and 6c, respectively). The preheat temperature was varied between 160 and 280 °C, and the cutheat temperature was 40 °C less than the preheat temperature. In Fig. 6b we show estimated natural doses from measurements as a function of preheat temperature. A plateau in the measured equivalent doses is observed in the preheat temperature range from 160 °C to 240 °C (dashed line). The average recycling ratio for this temperature range was 0.965±0.011 (n=15). At temperatures >240 °C the average doses increase significantly by ~ 30 Gy with preheat temperature. To assess the importance of thermal transfer (T) as a function of preheat temperature, a group of aliquots (n=18) were bleached twice for 100 s at room temperature (with an intervening pause of 10 ks) using the blue LEDs. The thermally transferred dose was subsequently measured using the SAR procedure and varying preheat temperatures (3 aliquots at each temperature) and the results are shown in Fig. 6d. These doses increase with preheat temperature from ~ 0.2 Gy to ~ 3 Gy, which is insufficient to explain the ~ 30 Gy difference observed in the natural preheat experiment (Fig. 6b). In the dose recovery preheat test, the aliquots were first bleached as in the thermal transfer experiment and subsequently given

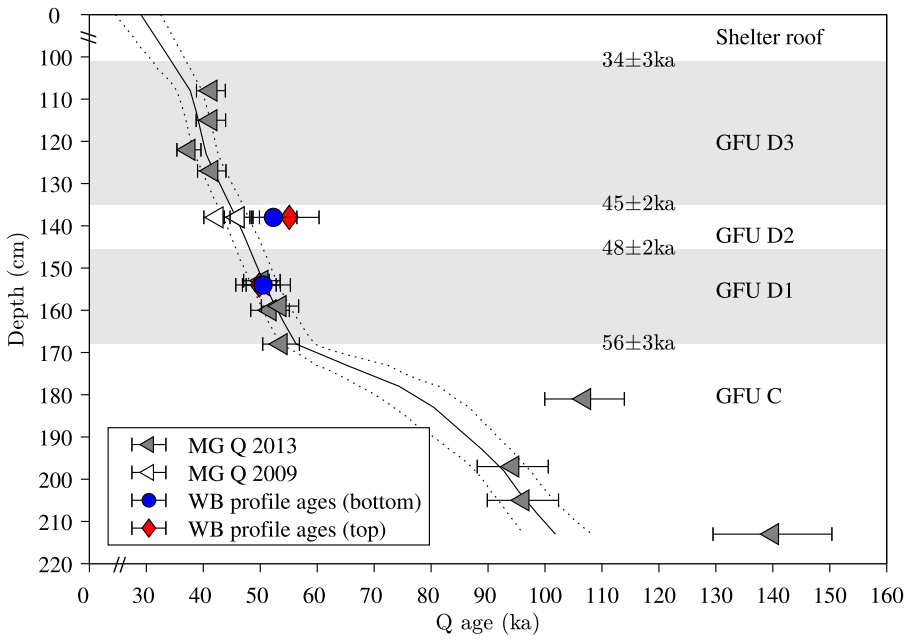

Fig. 8. Bordes-Fitte quartz luminescence ages vs depth. Sand-sized sediment (TA2248-61) multi-grain quartz ages are shown as triangles (MG Q 2013). Grey triangles show the sediment ages obtained in this work, whereas open triangles (MG Q 2009) are the multi-grain ages from Thomsen et al. (2016) from GFU D2. The sediment age for TA2247 is not shown as only a minimum age could be derived due to saturation effects. A Bayesian model (Bacon script Blaauw and Christen (2011)) using the depths as priors and only random uncertainties for the individual ages is shown (black line). Dotted black lines show the total uncertainty including both random and systematic uncertainties at 68% confidence. (Note that the systematic uncertainties are: the cosmic ray dose rate (5%), the internal alpha dose rate in quartz (0.01 Gy/ka), water content (4%), beta source calibration (2%) and dose rate systematics (2%) (see Murray et al., 2021, for further details). The position of the individual GFU layers are indicated and the modelled ages at the interfaces between the different units provided. Rock surface ages (circles and diamonds) are derived from slices identified to be well-bleached by the pre-burial profile (WB profile ages, see text for details). Cobbles ages from TA2266-68 (all GFU D2) have been averaged and both top (red diamonds) and bottom (blue circles) ages are shown. Uncertainties on all ages include both random and systematic contributions.

a known laboratory dose of ~ 67 Gy, close to the average equivalent dose measured for the surface grains for this sample. The measured-to-given dose ratios (after subtraction of the appropriate thermal transfer doses) do not vary significantly over the temperature range from 160 °C to 200 °C, where the average dose recovery ratio is 1.01±0.02 (n=9, see Fig. 6c). This shows that our protocol can accurately measure a known laboratory dose in this temperature range. The average D_c value is 105±5 Gy (n = 334) and so it is reasonable to assume that the protocol is applicable to at least $2 \times D_c$ ~ 210 Gy. Based on these results, a preheat temperature of 190 °C was chosen for further measurements; at this temperature the recuperation signal is small ($0.068\% \pm 0.015\%, n = 12$), the sensitivity change is $1.4 \pm 0.2, (n = 12)$, and the thermally transferred doses negligible compared to the surface equivalent doses ($0.3 \pm 0.2\%$ on average).

5.2. Sediment burial doses

The measured multi-grain quartz dose distributions for all samples (except TA2247 for which only 9 aliquots gave bounded dose estimates, see below) are shown as simple dose histograms in Fig. 7. Dose estimates rejected by the objective IQR criterion are shown in white. The main effect of applying the IQR criterion is to reject high dose outliers, but in some cases low dose outliers are also rejected. The average ratio between the arithmetic average doses with and without the application of the IQR criterion is 0.970±0.010 (n=15 samples). Thus, application of the IQR criterion does not significantly affect the average values, but it does reduce the uncertainty on the average equivalent dose by ~ 25%.

Table 4 summarises the equivalent dose, the number of accepted and rejected aliquots, the total dose rate (including the model corrections for heterogeneity in the gamma field, see Section 4.2) and the OSL burial age determined for each sample. The average equivalent dose for GFU D is ~ 120 Gy (n=10), for GFU C ~ 150 Gy (n=4) and for GFU B ~ 300 Gy (n=1). However, it is worth noting that of the 23 aliquots measured for sample TA2247 (GFU B) only 9 bounded dose estimates could be derived, i.e.~ 60% of the aliquots were discarded because of saturation effects. Thus, we consider it highly likely that the equivalent dose (and hence burial age) determined for this sample should be regarded as a minimum dose. The remaining samples all have equivalent doses less than 260 Gy, and fall in the range where the dose recovery ratios are acceptable (see Section 5.1.1). Thus, the OSL ages for these samples (GFU D3-C) are regarded as reliable.

5.3. Sediment burial ages

Fig. 8 shows the resulting multi-grain sediment ages with depth (triangles). The age for sediment sample TA2247 from GFU B is not included as it was concluded earlier that it is inaccurate due to saturation effects. The sediment burial ages are all consistent with stratigraphic order, although the age of sample TA2251 (107±6 ka) is only just consistent with the age of sample TA2250 (94±6 ka) taken 16 cm below TA2251. Based on these data, we consider it highly unlikely that unit GFU C was deposited in a single event; the uncertainties on the individual ages would have to be increased by more than 200% to allow the four sediment ages to become consistent with each other. For GFU D1 we obtained four OSL ages, which all are consistent with an average OSL age of 51.5±0.7 ka (n=4). The single sample taken from GFU D2 (TA2257) gives an OSL age of 46±2 ka. Previously measured multi-grain OSL ages (Thomsen et al., 2016) from GFU D2 give an average age of 44±2 ka (n=2) and are also shown in Fig. 8 (open triangles). This age is consistent with both the new burial age determined from this sampling campaign (i.e.TA2257, 46±2 ka) and with the Bayesian modelling results (see below). The four sediment ages obtained for GFU D3 are all consistent with the average age of 40.4 ± 1.0 ka (n=4).

5.4. Sediment depth-age modelling

We have modelled this depth-age relationship for the multi-grain quartz ages using Bayesian statistics with the sediment burial depths

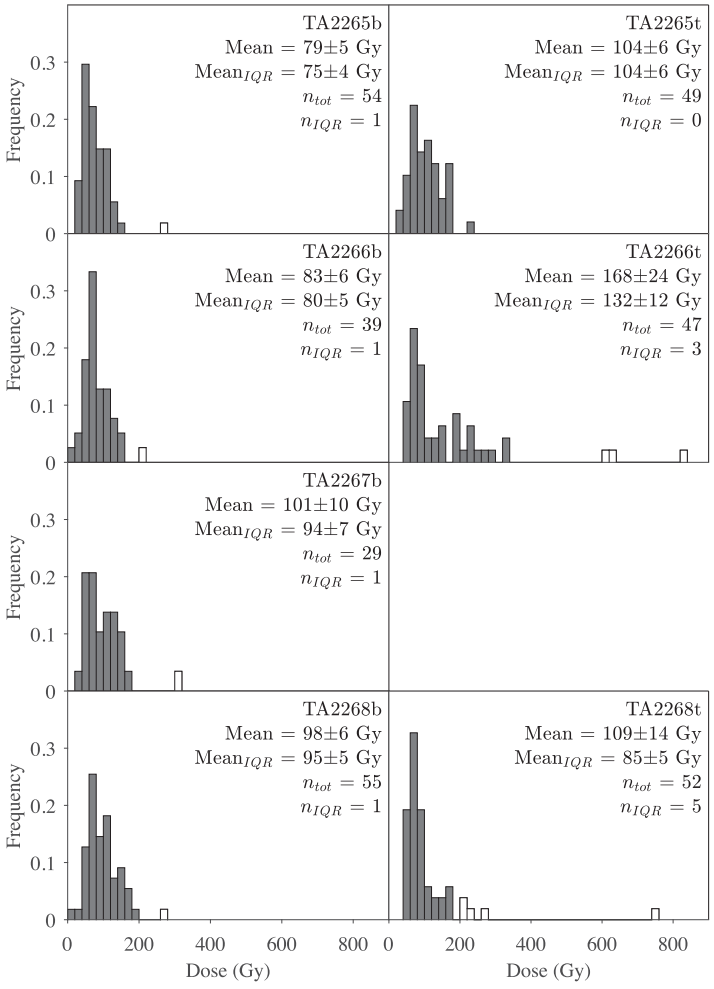

Fig. 9. Cobble multi-grain quartz dose distributions normalised to the total number of measured aliquots (n_{tot}) from both the top and the bottom of the individual cobbles (except sample TA2267). Dose estimates remaining after application of the IQR criterion are shown as grey bars, rejected data are shown as white bars. The legend for each sample gives the arithmetic mean dose and the standard error of all measured aliquots giving a bounded dose estimate. The total number of measured aliquots (n_{tot}) and the number of aliquots rejected by the IQR criterion are also given (n_{IQR}).

as priors (Bacon script, Blaauw and Christen (2011)). For modelling, only random uncertainties on the individual ages were used, although total (random and systematic) uncertainties are presented on each age in Fig. 8. The Bayesian model results are shown as a black solid line and the dashed lines around define the total uncertainty band (including both random and systematic uncertainties) at 68% confidence. The sediment ages are all consistent with the Bayesian model except two samples (TA2249 and TA2251) both from GFU C. Based on this model, unit GFU D3 was deposited between 40 ± 2 and 44 ± 2 ka, GFU D2 between 44 ± 2 and 48 ± 3 ka, GFU D1 between 48 ± 3 and 57 ± 3 ka and GFU C more than 57 ± 3 ka ago (all uncertainties are quoted at the 68% confidence level).

5.5. Rock surface burial ages

To derive burial ages from the four cobbles we have used two different approaches: (1) Measuring the burial dose for several surface slices only (i.e.depths < 1.2 mm; no deep coring was used to obtain these data) and (2) Measuring luminescence-depth profiles for the entire length of each cobble and using modelling of these profiles (Freiesleben et al., 2015) to obtain cobble burial estimates.

5.5.1. Rock surface burial ages from surface slices

One of the main advantages of rock surface burial dating when compared to standard sediment dating is that by measuring luminescence-depth profiles into the rock, one can directly estimate the degree of resetting of the luminescence signal at the rock surface at the time of burial. However, rock sample preparation (i.e.coring, slicing, chemical treatment) is labour intensive and from a single slice (ø 10 mm, thickness ~ 1.2 mm) there was only sufficient material to make ~ three 8 mm multi-grain aliquots. Given the observed scatter in quartz dose estimates, it is clearly desirable to obtain more material. In this study ~ 20 surface slices were taken from both the top and the bottom of each of the four cobbles without coring the full length of the cobbles. These slices were irregular in shape but had a mean thickness of 0.7±0.1mm. From cobble TA2267 only data from the bottom side is available, because this cobble was too fragile to extract slices, and the top surface did not have sufficient regular suitable locations from which to extract short cores. Our SAR protocol was used to measure the equivalent doses (D_e) recorded by grains extracted from slices from the cobble surfaces (top and bottom) and the resulting distributions of equivalent doses are shown in Fig. 9. Grey bars indicate dose estimates rejected by the IQR criterion. The dose distributions are generally symmetric around the average dose, except for the top of cobble TA2266, which appears to be significantly positively skewed. This is potentially a concern as it may indicate that this surface either was not bleached uniformly prior to burial or more likely that a part of the cobble surface had broken off (this surface was noticeable friable and grains could be rubbed off). For the remaining samples the average doses range between ~ 80 and 110 Gy and the resulting ages between ~ 48 and 80 ka (see Table 4). On average the surface slices overestimate the corresponding sediment

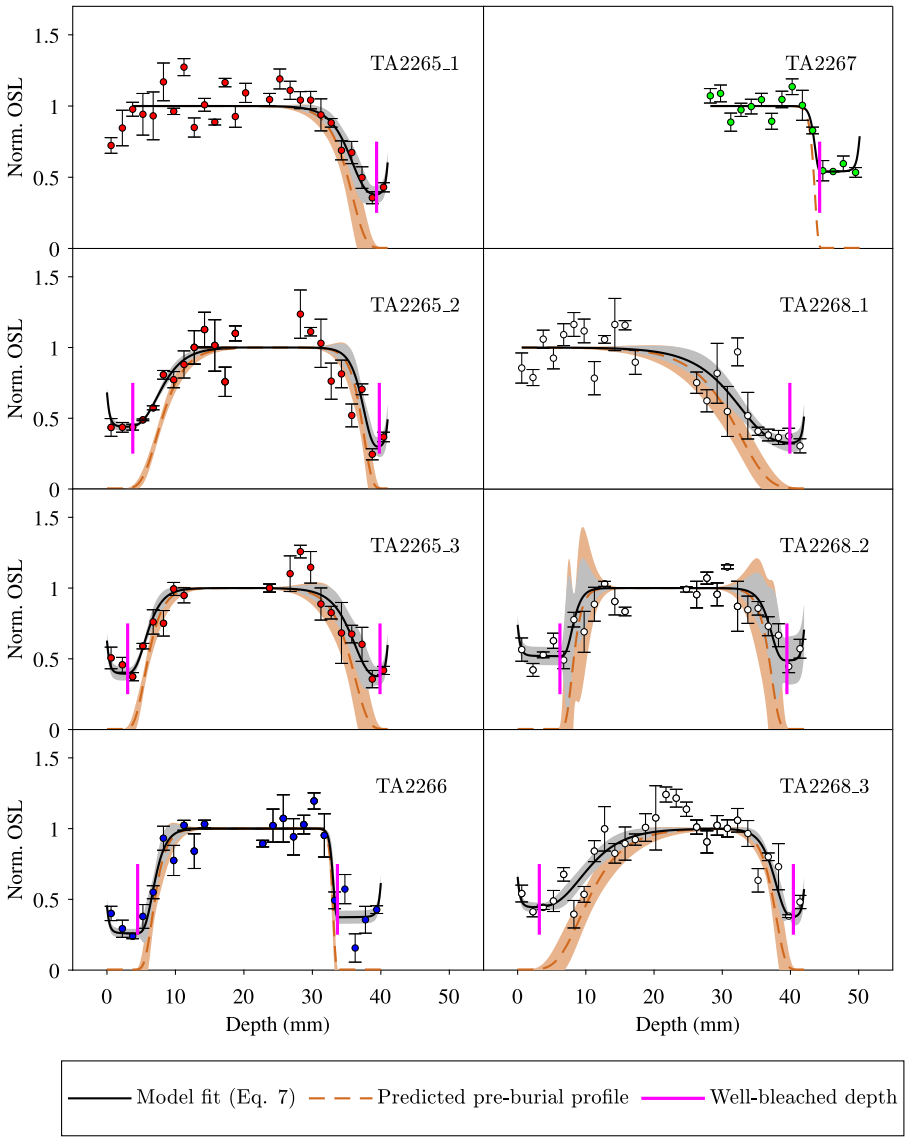

Fig. 10. Normalised sensitivity-corrected luminescence L_n/T_n profiles from cores drilled from buried surfaces from top ($x = 0$) to the bottom of cobbles TA2265-68. For some cobbles multiple cores were drilled and these are labelled _i, where i is 1, 2 or 3. The data have been normalised to the profile saturation value. Each data point is an average of the results from three aliquots. Uncertainties are one standard error. Fitting these data using the multiple event model (Freiesleben et al., 2015) with one exposure followed by a single burial (Eq. (7)) results in the full black lines with 68% confidence intervals (grey areas). The predicted pre-burial profiles (Eq. (6)) are shown as orange dashed lines and confidence intervals at 68% (orange areas). Vertical solid lines (magenta) indicate the depths to which the surfaces are predicted to have been well bleached (see text for details).

ages by 34±6% and 23±11% for the top and bottom sides, respectively, possibly indicating that at least the top sides of the cobbles were not well-bleached possibly because the cobbles were not intact.

5.5.2. Luminescence-depth profiles

As stated above, one of the major advantages of rock surface compared to sediment OSL dating is that rocks record information about past burial and exposure events. Such information can be extracted by applying appropriate mathematical models to measured luminescence-depth profiles, i.e.it is possible to directly assess whether the rock surface was well-bleached at burial. Here we have measured luminescence-depth profiles from top to bottom for all cobbles, except for cobble TA2267 where only the bottom part of the profile could be obtained. This was done by measuring natural sensitivity corrected OSL signals (L_n/T_n) from quartz grains extracted from individual rock slices obtained from one to three cores drilled completely through the cobbles (thickness of ~ 4 cm). The resulting profiles are shown in Fig. 10, where $x = 0$ is the top surface. At each depth, a minimum of three aliquots were measured.

A simple visual inspection of the profiles suggests that both the top and bottom of the cobbles have received a significant daylight exposure prior to burial. The only exceptions to this are the two top surfaces of TA2265_1 and TA2268_1 (at $x = 0$ mm).

Modelling is required to obtain an analytical description of the luminescence-depth profiles and the variation of total dose rate with depth. Sohbati et al. (2012a) suggested a first-order model which describes the resetting of the OSL signal with depth during a single bleaching event (Eq. (6), excluding trap refilling during light exposure). Freiesleben et al. (2015) expanded this model to include multiple sequential exposure and burial events in a unified equation (Eq. (7) for a single exposure and burial event), where Eq. (6) is the initial condition (n_1) in Eq. (7).

$$n_1(x, t_e) = n_0 e^{-\overline{\sigma\varphi_0} t_e e^{-\mu x}} \tag{6}$$

$$n_2(x, t_e, t_b) = (1 - T)\left((n_1 - 1)e^{\frac{-\dot{D}(x)}{D_c} t_b} + 1\right) + T \tag{7}$$

where $\overline{\sigma\varphi_0}$ [ka^{-1}] is the detrapping rate constant at the surface of the cobble averaged over all wavelengths in the light spectrum reaching the

sample, σ [cm^2] is the photoionisation cross section, φ [cm^{-2} ka^{-1}] is the incoming photon flux, and μ [mm^{-1}] is the inverse of the mean free path of photons in the cobble, assumed to be constant with depth. For the buried surfaces, t_b (ka) is the time elapsed since final burial, whereas t_e is the preburial exposure time (ka), $\dot{D}(x)$ is the dose rate (Gy ka^{-1}, see Eq. (1)), and D_c characterises the rate of trapping, so that $\dot{D}(x)/D_c$ is the probability of trap filling per unit time. Note that thermal transfer is included in the model as T.

Eq. (7) (using the dose rate depth dependence described in Eq. (1)) is used to fit the measured data. The resulting fits are shown in Fig. 10 as black lines (the grey uncertainty band is drawn at 68% confidence). Using the best-fit parameter values of μ and $\overline{\sigma\varphi_0}t_e$ in Eq. (6), the pre-burial profile (see dashed orange line in Fig. 10) can be determined. Visual inspection of these pre-burial profiles indicate that all surfaces were well-bleached at burial (excluding the top surfaces of TA2265_1 and TA2268_1), i.e.these pre-burial profiles are "flat" and close to zero near the surfaces. However, the degree of bleaching of the cobble surfaces before burial can be formally estimated using the fitting parameters obtained to predict the shape of the pre-burial luminescence profile. To determine whether a surface is well-bleached we define the following criterion: the rock surfaces were well-bleached to the depth where the value of the predicted pre-burial profile ($n_1(x)$) is less than 5% of the light level after burial at same depth, i.e.where $n_1(x) + se - T \leq 0.05 \times (L_{n,s}/T_{n,s}(x) - T)$, where se is the half width of the confidence band and T is thermal transfer.

The resulting depths are shown as magenta solid vertical lines in Fig. 10. All aliquots from these depths or shallower are considered to be well-bleached. Doses measured from these aliquots are therefore considered reliable (at least from the point of view of bleaching) and used to determine burial ages.

Burial ages determined from these depths are not significantly different from the burial ages determined from the corresponding surface slice from same core (at 95% confidence), although the ages derived particularly from bottom of TA2266 (i.e. TA2266b) are scattered and poorly known (see Table 5). Thus, we conclude that all bottom surfaces were well-bleached to a depth including, at least, the first data point. On the other hand, two of the luminescence profiles from the top surfaces (TA2265_1 and TA2268_1) indicate that at least some parts of these surfaces were either not significantly bleached at burial and/or have suffered from erosion (Sohbati et al., 2018), such that the well-bleached part has been removed. Assuming that all well-bleached ages estimated from the same sample and the same side come from the same distribution we apply the inter quartile rejection criteria to all ages (top and bottom) from each sample. The resulting distributions are seen in Fig. 11 with grey bars indicating accepted ages and white bars indicating rejected ages. The arithmetic mean age (calculated without application of the IQR criterion) and its standard error (random only) of all measured aliquots are given in the legends.

To further support the conclusion that some parts of the top sides from samples TA2265 and TA2268 were probably not well-bleached, we compare ages from the top and bottom for each cobble (see Fig. 12a, black squares). Only for one cobble (TA2265) is there good agreement between the top and bottom. In Fig. 12a, we also compare the top and bottom ages for all surface slices (pink triangles, see also Table 4) and again observe a relatively poor agreement between top and bottom ages, except for cobble TA2268. In Fig. 12b, we compare the surface slice ages with the well-bleached profile ages. For the bottom sides, there is a good agreement between the surface ages (Table 4) and the well-bleached profile ages (Table 5) with an average ratio of 1.12±0.16 (n=4) (blue circle points). Only for cobble TA2268 are the two ages not consistent with each other (ratio of 1.53±0.17). However, for the top sides (red diamond symbols), the results are highly scattered with an average ratio of 1.6±0.5 (n=3). The agreement is particularly poor for cobble TA2266, which has a surface slice age of 80±8 (n=47) and a profile age of 33±2 ka (n=15). For the top sides the poor agreement probably indicates that different parts of the cobble surfaces experienced different bleaching histories and/or that the surfaces were not intact. Thus, subsequently we only use burial ages derived from cores where the profiles have been identified to be well-bleached at burial. We conclude that the ages derived from surface slices exclusively (i.e.only the first 1.2 mm and not the full profile, see Table 4) are not accurate.

5.5.3. Well-bleached rock surface burial ages

All the profiles that we have used to derive ages from the tops and bottoms of these rocks have been identified as well bleached. For the rock sample TA2265 from unit D1 the top and bottom ages are consistent and give an average age of 50±3 ka (n=44). For the two rock samples from unit D2 (TA2266 and -68) for which we have both top and bottom ages, these are not consistent. For sample TA2266 the top age of 33±3 ka is significantly younger than the bottom age of 62±12 ka. This sample was taken from the top of GFU D2 and so it is possible that it records the deposition of the overlying GFU D3, however the average sediment age, 40.4 ± 1.0 ka, is significantly older. In the other case of rock TA2268 the surface age of 74 ± 7 ka is significantly older than the bottom age of 43 ± 4 ka. This rock was also sampled from the top of GFU D2. Thus, this older top age is difficult to accept because it would require that after complete bleaching the rock remained completely unexposed for approximately 30 ka even although it ended up on the top of GFU D2. Thus, although we cannot rule out the possibility that the various ages recorded by the top and bottoms of these two rocks do indeed record different events, it seems much more likely that these differences in age result from variability in our measurements and so should be treated as estimates of the age of a single event. It is also interesting to note that the average of the ages of the top surfaces (54 ka) is very similar the two bottom surfaces (53 ka).

In Fig. 8, we show the average layer cobble-burial ages from profiles determined to have been well-bleached at burial (both bottom and top sides), i.e.for GFU D1 (TA2265) a cobble age of 50 ± 3 ka (n = 44) and for GFU D2 (TA2266-68) a cobble age of 54 ± 4 ka (n = 76). Both of these ages are consistent with the corresponding sediment multi-grain quartz ages, i.e.51.5±0.7 ka (n=4 samples from GFU D1) and 46±2 ka (n=1 sample from GFU D2) and the Bayesian depth-age model based on the sediment ages (TA2248-61).

6. Discussion and conclusion

The main purposes of this study were both to establish a reliable absolute OSL chronology for the lower layers (i.e.GFU D3-B) at the Les Roches D'Abilly site and to test the accuracy of this chronology using OSL rock surface luminescence dating on four cobbles found in GFU D1 and D2. The resulting OSL multi-grain quartz chronology is considered to be robust and reliable with all ages consistent with stratigraphic order (although sample TA2251 at 181 cm (107±6 ka) is only just consistent with sample TA2250 (94±6 ka) at 197 cm). No bounded OSL age could be derived from the single sample taken in GFU B (TA2247) as the OSL signal appeared to be saturated. The sediment OSL age derived for layer GDF D2 (46±2 ka) is in excellent agreement both with previously published OSL ages for this unit and with radiocarbon ages for GFU D2 (age range 45.1–41.5 ka cal BP at 95% confidence, Thomsen et al. (2016)). For layer GFU D1 the four OSL ages increase systematically with depth but are all consistent with an average OSL age of 51.5±0.7 ka (n=4). The Bayesian depth-age model for the sand-sized sediment ages (see Fig. 8) indicates that the sterile layer GFU D3 was deposited rapidly between 40±2 ka and 44±2 ka ago before the Auriginacian occupation (AMH) of the site. Similarly, GFU D2 containing Châtelperronian blades on top of tools produced by the Discoidal reduction scheme was deposited between 44±2 ka and 48±3 ka ago. Thus, the technological change from Discoidal to blade production occurred in this time range. GFU D1 (containing lithic assemblages obtained using Levallois recurrent and lineal methods) was deposited between 48±3 ka and 57±3 ka ago. Independent age control

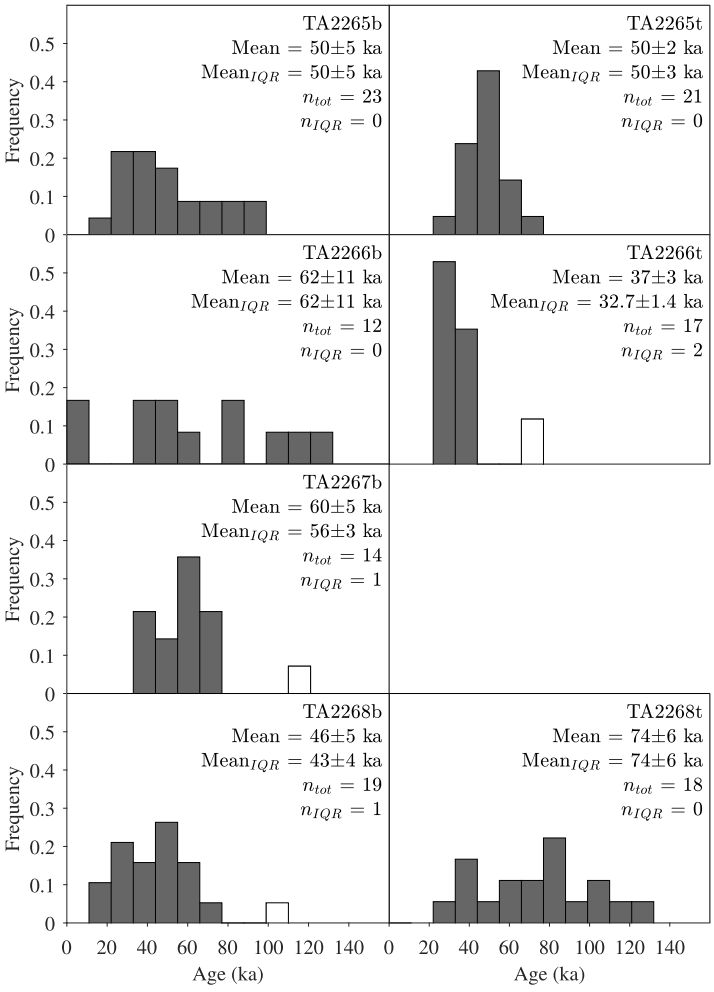

Fig. 11. Cobble multi-grain quartz normalised age distributions from well-bleached depths, from both the top and the bottom of the individual cobbles (except sample TA2267t). Because the individual aliquots come from different depths with slightly different dose rates (see Table 5) it is necessary to average ages rather than equivalent doses. Ages after application of the IQR criterion are shown as grey bars, whereas ages estimates rejected by the IQR criterion are shown as white bars. The legend for each sample gives the arithmetic mean age and standard error of all measured aliquots (i.e.without application of the IQR criterion) giving a bounded dose estimate. Also given is the arithmetic mean after including application of the IQR criterion (Mean$_{IQR}$). The total number of measured aliquots (n_{tot}) and the number of aliquots rejected by the IQR criterion (n_{IQR}) is also shown.

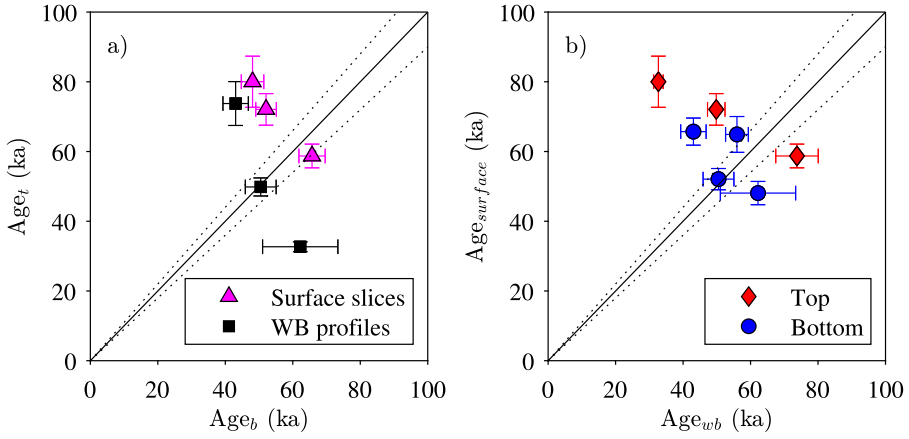

Fig. 12. (a) Comparison between cobble ages derived from the top and bottom sides of each cobble derived from surface slices only (pink triangles), and ages derived from slices determined to be well-bleached using modelling of luminescence-depth profiles (black squares). (b) Comparison between well-bleached profile ages and surface ages, respectively from the top (red diamonds) and the bottom (blue circles) sides of the cobbles, respectively. Only random uncertainties are included in this comparison. The IQR criterion was applied to all data sets.

from ^{14}C exists for four GFU levels (F, E, D2 and D1). Five ^{14}C AMS ages gives an age span of 45.1–41.5 ka cal BP for GFU D2, which is in good agreement with the ages derived from the Bayesian OSL depth-age model. For GFU D1 a single ^{14}C AMS age of 48.4–42.7 ka cal BP (at 95%) is available. Although this age is strictly consistent with the Bayesian OSL age range of 48±3 to 57±3 ka, unless the ^{14}C samples was taken at the very top of the unit, it probably underestimates the age. We regard the OSL ages for this unit as more reliable, because underestimation by ^{14}C in this age range is widely recognised (Jacobi et al., 2006; Song et al., 2018; Zilhão et al., 2021; Devièse et al., 2021).

Considerable qualitative information on the daylight exposure and burial history of the rock samples was obtained by measuring optically stimulated luminescence at different depths in four cobbles. The underlying luminescence profiles were investigated and well-bleached rock surfaces identified, and thus dated with confidence. Using luminescence-depth modelling, insight into the degree of bleaching prior to the burial event was obtained. In this study, it has proved possible to derive rock surface burial ages from 1 cm diameter cores drilled through the cobbles from top to bottom. Our data and modelling suggest that the bottom sides of the cobbles from Les Roches D'Abilly were all well-bleached before burial. The top sides were in some parts of the cobbles determined to be well-bleached but in other parts incompletely bleached. The latter presumably arose either because the cobble surfaces were not exposed uniformly to light prior to burial or, more likely, parts of the surfaces broke off either shortly before burial or some time there after. Sampling cobble luminescence-depth profiles is labour intensive, and we also investigated whether accurate burial ages could be obtained by simply measuring surface slices. The average of all burial ages obtained from such surface slices from the bottom sides of the cobbles are in good agreement with those derived from profiles determined to have been well-bleached. However, the use of surface slices from the upper surfaces tends to overestimate those derived from well-bleached profiles. This suggest a different bleaching history for some parts of the top surfaces; as a result we only draw conclusions from the known well-bleached profiles, rather than including all the measured top surface slices. The burial ages obtained from rock surfaces are in good agreement with the ages obtained by standard multi-grain quartz OSL dating methods for the sediments.

Well-bleached rock surfaces give 50 ± 3 ka and 54 ± 4 ka for level D1 and D2, respectively, consistent with the Bayesian depth-age model based on multi-grain quartz sand-sized sediment ages of 51.5 ± 0.7 ka (depth 153–160 cm) and 46 ± 2 ka (depth 138 cm) for level D1 and D2 respectively.

This study serves to confirm the suggestion that rock surfaces contain a record of exposure and burial history. It also demonstrates the value of luminescence-depth profiles when used to test the assumption of complete bleaching. Such direct bleaching information is not available in standard optically stimulated luminescence sediment dating.

Declaration of competing interest

The authors declare that they have no known competing financial interests or personal relationships that could have appeared to influence the work reported in this paper.

Data availability

Data will be made available on request.

Acknowledgements

We thank Joy Mailand-Hansen and Vicki Hansen for assistance with the sample preparation. Reza Sohbati would like to thank Carlsberg Foundation, Denmark for financial support (Grant No. : 2012-01-0838) during part of this project. The Centre for Viscous Liquid Dynamics "Glass and Time" is sponsored by the Danish National Research Foundation via grant DNRF61.

References

Ageby, L., Angelucci, D.E., Brill, D., Carrer, F., Rades, E.F., Rethemeyer, J., Brückner, H., Klasen, N., 2021. Rock surface IRSL dating of buried cobbles from an alpine dry-stone structure in Val di Sole, Italy. Quat. Geochronol. 66, 101212.
Aitken, M.J., 1985. Thermoluminescence Dating. AP.
Aitken, M.J., 1998. An Introduction to Optical Dating. OUP, Oxford.
al Khasawneh, S., Abu-Jaber, N., Hamarneh, C., Murray, A., 2022. Age determination of runoff terrace systems in Petra, Jordan, using rock surface luminescence dating. Archaeol. Anthropol. Sci. 14, 48.
al Khasawneh, S., Murray, A.S., Abudanah, F., 2019. A first radiometric chronology for the Khatt Shebib megalithic structure in Jordan using the luminescence dating of rock surfaces. Quat. Geochronol. 49, 205–210, 15th International Conference on Luminescence and Electron Spin Resonance Dating, 11-15 September 2017, Cape Town, South Africa.
al Khasawneh, S., Murray, A., Thomsen, K., AbuAzizeh, W., Tarawneh, M., 2018. Dating a near eastern desert hunting trap (kite) using rock surface luminescence dating. Archaeol. Anthropol. Sci. 11 (5).
Aubry, T., Dimuccio, L.A., Almeida, M., Buylaert, J.-P., Fontana, L., Higham, T., Liard, M., Murray, A.S., Neves, M.J., Peyrouse, J.-B., Walter, B., 2012. Stratigraphic and technological evidence from the middle palaeolithic-Châtelperronian-Aurignacian record at the Bordes-Fitte rockshelter (Roches d'Abilly site, Central France). J. Hum. Evol. 62 (1), 116–137.
Aubry, T., Dimuccio, L.A., Barbosa, A.F., Luís, L., Santos, A.T., Silvestre, M., Thomsen, K.J., Rades, E., Autzen, M., Murray, A.S., 2020. Timing of the middle-to-upper palaeolithic transition in the Iberian inland (Cardina-Salto do Boi, Côa Valley, Portugal). Quat. Res. 98, 81–101.
Aubry, T., Dimuccio, L.A., Buylaert, J.-P., Liard, M., Murray, A.S., Thomsen, K.J., Walter, B., 2014. Middle-to-upper Palaeolithic site formation processes at the Bordes-Fitte rockshelter (Central France). J. Archael. Sci. 52, 436–457.
Bailiff, I., Bridgland, D., Cunha, P.P., 2021. Extending the range of optically stimulated luminescence dating using vein-quartz and quartzite sedimentary pebbles. Quat. Geochronol. 65, 101180.
Ballarini, M., Wallinga, J., Wintle, A.G., Bos, A.J.J., 2007. A modified SAR protocol for optical dating of individual grains from young quartz samples. Radiat. Meas. 42, 360–369.
Banerjee, D., Murray, A.S., Bøtter-Jensen, L., Lang, A., 2001. Equivalent dose estimation using a single aliquot of polymineral fine grains. Radiat. Meas. 33, 73–94.
Blaauw, M., Christen, J.A., 2011. Flexible paleoclimate age-depth models using an autoregressive gamma process. Bayesian Anal. 6, 457–474.
Bøtter-Jensen, L., Thomsen, K.J., Jain, M., 2010. Review of optically stimulated luminescence (OSL) instrumental developments for retrospective dosimetry. Radiat. Meas. 45, 253–257.
Chapot, M.S., Sohbati, R., Murray, A.S., Pederson, J.L., Rittenour, T.M., 2012. Constraining the age of rock art by dating a rockfall event using sediment androck-surface luminescence dating techniques. Quat. Geochronol. 13, 18–25.
Cresswell, A., Carter, J., Sanderson, D., 2018. Dose rate conversion parameters: Assessment of nuclear data. Radiat. Meas. 120, 195–201, 15th International Conference on Luminescence and Electron Spin Resonance Dating, 11-15 September 2017.
Cresswell, A., Sanderson, D., Carter, J., 2019. Review of nuclear data for naturally occurring radionuclides applied to environmental applications. Eur. Phys. J. Plus 134 (69).
Cunningham, A., Khashchevskaya, D., Semikolennykh, D., Kurbanov, R., Murray, A., 2022. Luminescence dating of mass-transport sediment using rock-surface burial methods: A test case from the Baksan valley in the Caucasus mountains. Quat. Geochronol. 68, 101253.
Devièse, T., Abrams, G., Hajdinjak, M., Pirson, S., De Groote, I., Di Modica, K., Toussaint, M., Fischer, V., Comeskey, D., Spindler, L., Meyer, M., Semal, P., Higham, T., 2021. Reevaluating the timing of neanderthal disappearance in Northwest Europe. Proc. Natl. Acad. Sci. USA 118 (12).
Duller, G., 2008a. Luminescence Dating: Guidelines on using Luminescence Dating in Archaeology. Engl. Herit., Swindon.
Duller, G.A.T., 2008b. Single-grain optical dating of quaternary sediments: Why aliquot size matters in luminescence dating. Boreas 37, 589–612.
Freiesleben, T.H., 2021. Developing and Testing Models for Rock Surface Dating Using Optically Stimulated Luminescence (Ph.D. Thesis). Technical University of Denmark, http://ancienttl.org/theses.htm.
Freiesleben, T.H., Sohbati, R., Murray, A.S., Jain, M., Hvidt, S., Jakobsen, B., 2015. Mathematical model quantifies multiple daylight exposure and burial events for rock surfaces using luminescence dating. Radiat. Meas. 81, 16–22.
Galli, A., Martini, M., Maspero, F., Panzeri, L., Sibilia, E., 2014. Surface dating of bricks, an application of luminescence techniques. Eur. Phys. J. Plus 129, 101.
Galli, A., Panzeri, L., Rondini, P., Keller, R.P., Martini, M., 2020. Luminescence dating of rock surface. The case of Monoliths from the Megalithic sanctuary of Ossimo-Pat (Valle Camonica, Italy). Appl. Sci. 10, 7403.
Gliganic, L.A., Meyer, M.C., May, J.-H., Aldenderfer, M.S., Tropper, P., 2021. Direct dating of lithic surface artifacts using luminescence. Sci. Adv. 7 (23).
Gravina, B., Bachellerie, F., Caux, S., Discamps, E., Faivre, J.-P., Galland, A., Michel, A., Teyssandier, N., Bordes, J.-G., 2018. No reliable evidence for a Neanderthal-Châtelperronian association at La Roche-à-Pierrot, Saint-Césaire. Sci. Rep. 8, 15134.

Greilich, S., Glasmacher, U.A., Wagner, G.A., 2005. Optical dating of granitic stone surfaces. Archaeometry 47, 645–665.

Guérin, G., Christophe, C., Philippe, A., Murray, A.S., Thomsen, K.J., Tribolo, C., Urbanova, P., Jain, M., Guibert, P., Mercier, N., Kreutzer, S., Lahaye, C., 2017. Absorbed dose, equivalent dose, measured dose rates, and implications for OSL age estimates: Introducing the average dose model. Quat. Geochronol. 41, 163–173.

Guérin, G., Mercier, N., Adamiec, G., 2011b. Dose-rate conversion factors: Update. Ancient TL 29, 5–8.

Guérin, G., Mercier, N., Nathan, R., Adamiec, G., Lefrais, Y., 2012. On the use of the infinite matrix assumption and associated concepts: A critical review. Radiat. Meas. 47 (9), 778–785.

Habermann, J., Schilles, T., Kalchgruber, R., Wagner, G.A., 2000. Steps towards surface dating using luminescence. Radiat. Meas. 32 (5–6), 847–851.

Hansen, V., Murray, A.S., Buylaert, J.-P., Yeo, E.Y., Thomsen, K.J., 2015. A new irradiated quartz for beta source calibration. Radiat. Meas. 81, 123–127.

Higham, T., Douka, K., Wood, R., Ramsey, C.B., Brock, F., Basell, L., Camps, M., Arrizabalaga, A., Baena, J., Barroso-Ruíz, C., Bergman, C., Boitard, C., Boscato, P., Caparrós, M., Conard, N., Draily, C., Froment, A., Galván, B., Gambassini, P., Garcia-Moreno, A., Grimaldi, S., Haesaerts, P., Holt, B., Iriarte-Chiapusso, M.-J., Jelinek, A., Pardo, J.F.J., Maíllo-Fernández, J.-M., Marom, A., Maroto, J., Menéndez, M., Metz, L., Morin, E., Moroni, A., Negrino, F., Panagopoulou, E., Peresani, M., Pirson, S., de la Rasilla, K., Riel-Salvatore, J., Ronchitelli, A., Santamaria, D., Semal, D., Slimak, L., Soler, J., Soler, N., Villaluenga, A., Pinhasi, R., Jacobi, R., 2014. The timing and spatiotemporal patterning of Neanderthal disappearance. Nature 512, 306–309.

Higham, T., Jacobi, R., Julien, M., David, F., Basell, L., Wood, R., Davies, W., Ramsey, C.B., 2010. Chronology of the grotte du renne (France) and implications for the context of ornaments and human remains within the Châtelperronian. Proc. Natl. Acad. Sci. USA 107 (47), 20234–20239.

Hublin, J.-J., Talamo, S., Julien, M., David, F., Connet, N., Bodu, P., Vandermeersch, B., Richards, M.P., 2012. Radiocarbon dates from the Grotte du Renne and Saint-Césaire support a Neandertal origin for the hâtelperronian. Proc. Natl. Acad. Sci. USA 109 (46), 18743–18748.

Ishii, Y., Takahashi, T., Ito, K., 2022. Luminescence dating of cobbles from pleistocene fluvial terrace deposits of the Ara River, Japan. Quat. Geochronol. 67, 101228.

Jacobi, R.M., Higham, T.F.G., Ramsey, C.B., 2006. AMS radiocarbon dating of middle and upper Palaeolithic bone in the British isles: Improved reliability using ultrafiltration. J. Quat. Sci. 21 (5), 557–573.

Jenkins, G.T.H., Duller, G.A.T., Roberts, H.M., Chiverrell, R.C., Glasser, N.F., 2018. A new approach for luminescence dating glaciofluvial deposits - high precision optical dating of cobbles. Quat. Sci. Rev. 192, 263–273.

Laskaris, N., Liritzis, I., 2011. A new mathematical approximation of sunlight attenuation in rocks for surface luminescence dating. J. Lumin. 131, 1874–1884.

Liritzis, I., 1994. A new dating method by thermoluminescence of carved megalithic stone building. C.R. Acad. Sci. Ser. II 319, 603–610.

Liritzis, I., 2011. Surface dating by luminescence: An overview. Geochronometria 38, 292–302.

Liritzis, I., Aravantinos, V., Polymeris, G.S., Zacharias, N., Fappas, I., Agiamarniotis, G., Sfampa, I.K., Vafiadou, A., Kitis, G., 2015. Witnessing prehistoric Delphi by luminescence dating. C. R. Palevol. 14 (3), 219–232.

Liritzis, I., Bednarik, R., Kumar, G., Polymeris, G., Iliopoulos, I., Xanthopoulou, V., Zacharias, N., Vafiadou, A., Bratitsi, M., 2018. Daraki-Chattan rock art constrained OSL chronology and multianalytical techniques: Afirst pilot investigation. J. Cult. Herit. 37, 29–43.

Liritzis, I., Panou, E., Exarhos, M., 2017. Novel approaches in surface luminescence dating of rock art: A brief review. Mediterr. Archaeol. Archaeom. 17 (4), 89–102.

Liritzis, I., Polymeris, G.S., Vafiadou, A., Sideris, A., Levy, T.E., 2019. Luminescence dating of stone wall, tomb and ceramics of Kastrouli (Phokis, Greece) late helladic settlement: Case study. J. Cult. Herit. 35, 76–85, Modern and Contemporary Art.

Liritzis, I., Polymeris, S., Zacharias, N., 2010. Surface luminescence dating of 'dragon houses' and Armena gate at Styra (Euboea, Greece). Mediterr. Archaeol. Archaeom. 10 (3), 65–81.

Liritzis, I., Vafiadou, A., 2015. Surface luminescence dating of some Egyptian monuments. J. Cult. Herit. 16 (2), 134–150.

Liritzis, I., Zacharias, N., Al-Otaibi, F., Iliopoulos, I., Katagas, C., Shaltout, M., 2016. Chronology of construction and occupational phases of Nawamis tombs, Sinai based on OSL dating. Geochronometria 43 (1), 121–130.

Medialdea, A., Thomsen, K.J., Murray, A.S., Benito, G., 2014. Reliability of equivalent-dose determination and age-models in the OSL dating of historical and modern palaeoflood sediments. Quat. Geochronol. 22, 11–24.

Murray, A.S., Buylaert, J.-P., Guérin, G., Qin, J., Singhvi, A.K., Smedley, R.S., Thomsen, K.J., 2021. Optically stimulated luminescence dating using quartz sand. Nat. Rev. Methods 1 (1), 1–31.

Murray, A.S., Helsted, L.M., Autzen, M., Jain, M., Buylaert, J.-P., 2018. Measurement of natural radioactivity: Calibration and performance of a high-resolution gamma spectrometry facility. Radiat. Meas. 120, 215–220.

Murray, A.S., Marten, R., Johnston, A., Martin, P., 1987. Analysis for naturally occurring radionuclides at environmental concentrations by gamma spectrometry. J. Radioanalytical Nucl. Chem. 115, 263–288.

Murray, A.S., Thomsen, K.J., Masuda, N., Buylaert, J.-P., Jain, M., 2012. Identifying well-bleached quartz using the different bleaching rates of quartz and feldspar luminescence signals. Radiat. Meas. 47, 688–695.

Murray, A.S., Wintle, A.G., 2000. Luminescence dating of quartz using an improved single-aliquot regenerative-dose protocol. Radiat. Meas. 32, 57–73.

Murray, A.S., Wintle, A.G., 2003. The single aliquot regenerative dose protocol: Potential for improvements in reliability. Radiat. Meas. 37, 377–381.

Olley, J.M., Caitcheon, G., Roberts, R.G., 1999. The origin of dose distributions in fluvial sediments, and the prospect of dating single grains from fluvial deposits using optically stimulated luminescence. Radiat. Meas. 30, 207–217.

Polikreti, K., Michael, C., Maniatis, Y., 2002. Authenticating marble sculpture with thermoluminescence. Ancient TL 20, 11–18.

Polikreti, K., Michael, C.T., Maniatis, Y., 2003. Thermoluminescence characteristics of marble and dating of freshly excavated marble objects. Radiat. Meas. 37 (1), 87–94.

Prescott, J.R., Hutton, J.T., 1994. Cosmic ray contributions to dose rates for luminescence and ESR dating: Large depths and long-term variations. Radiat. Meas. 23, 497–500.

Puttagan, T., Chawchai, S., Surakiatchai, P., Chalorsantisakul, S., Preusser, F., 2019. Luminescence dating of brick constructions being part of Songkhla City Wall, Southern Thailand. Archaeol. Anthropol. Sci. 11, 5393–5403.

Rades, E.F., Sohbati, R., Lüthgens, C., Jain, M., Murray, A.S., 2018. First luminescence-depth profiles from boulders from moraine deposits: Insights into glaciation chronology and transport dynamics in Malta valley, Austria. Radiat. Meas. 120, 281–289, 15th International Conference on Luminescence and Electron Spin Resonance Dating, 11-15 September 2017.

Reimer, P.J., Austin, W.E.N., Bard, E., Bayliss, A., Blackwell, P.G., Bronk Ramsey, C., Butzin, M., Cheng, H., Edwards, R.L., Friedrich, M., Grootes, P., Guilderson, T., Hajdas, I., Heaton, T., Hogg, A., Hughen, K., Kromer, B., Manning, S., Muscheler, R., Palmer, J., Pearson, C., van der Plicht, J., Reimer, R., Richards, D., Scott, E., Southon, J., Turney, C., Wacker, L., Adolphi, F., Büntgen, U., Capano, M., Fahrni, S., Fogtmann-Schulz, A., Friedrich, R., Köhler, P., Kudsk, S., Miyake, F., Olsen, J., Reinig, F., Sakamoto, M., Sookdeo, A., Talamo, S., 2020. The IntCal20 northern hemisphere radiocarbon age calibration curve (0–55 cal kBP). Radiocarbon 62 (4), 725–757.

Riedesel, S., Autzen, M., 2020. Beta and gamma dose rate attenuation in rocks and sediment. Radiat. Meas. 133 (106295).

Rosato, A., Strandburg, K.J., Prinz, F., Swendsen, R.H., 1987. Why the Brazil nuts are on top: Size segregation of particulate matter by shaking. Phys. Rev. Lett. 58, 1038–1040.

Sellwood, E.L., Guralnik, B., Kook, M., Prasad, A.K., Sohbati, R., Hippe, K., Wallinga, J., Jain, M., 2019. Optical bleaching front in bedrock revealed by spatially-resolved infrared photoluminescence. Sci. Rep. 9, 2611.

Simms, A.R., DeWitt, R., Kouremenos, P., Drewry, A.M., 2011. A new approach to reconstructing sea levels in Antarctica using optically stimulated luminescence of cobble surfaces. Quat. Geochronol. 6 (1), 50–60.

Singh, A., Thomsen, K.J., Sinha, R., Buylaert, J.-P., Carter, A., Mark, D.F., Mason, P.J., Densmore, A.L., Murray, A.S., Jain, M., Paul, D., Gupta, S., 2017. Counter-intuitive influence of himalayan river morphodynamics on Indus civilisation urban settlements. Nature Commun. 8, 1–14.

Slimak, L., Zanolli, C., Higham, T., Frouin, M., Schwenninger, J.-L., Arnold, L.J., Demuro, M., Douka, K., Mercier, N., Guérin, G., Valladas, H., Yvorra, P., Giraud, Y., Seguin-Orlando, A., Orlando, L., Lewis, J.E., Muth, X., Camus, H., Vandevelde, S., Buckley, M., Mallol, C., Stringer, C., Metz, L., 2022. Modern human incursion into Neanderthal territories 54,000 years ago at Mandrin, France. Sci. Adv. 8 (6), eabj9496.

Sohbati, R., 2013. Luminescence, rock surfaces. In: Encyclopedia of Scientific Dating Methods, vol. 221.

Sohbati, R., Jain, M., Murray, A.S., 2012a. Surface exposure dating of non-terrestrial bodies using optically stimulated luminescence: A new method. Icarus 221, 160–166.

Sohbati, R., Liu, J., Jain, M., Murray, A., Egholm, D., Paris, R., Guralnik, B., 2018. Centennial- to millennial-scale hard rock erosion rates deduced from luminescence-depth profiles. EPSL 493, 218–230.

Sohbati, R., Murray, A.S., Buylaert, J.-P., Almeida, N.A.C., Cunha, P.P., 2012b. Optically stimulated luminescence (OSL) dating of quartzite cobbles from the Tapada do Montinho archaeological site (east-central Portugal). Boreas 41, 452–462.

Sohbati, R., Murray, A.S., Jain, M., Buylaert, J.-P., Thomsen, K.J., 2011. Investigating the resetting of OSL signals in rock surfaces. Geochronometria 38, 249–258.

Sohbati, R., Murray, A.S., Porat, N., Jain, M., Avner, U., 2015. Age of a prehistoric "Rodedian" cult site constrained by sediment and rock surface luminescence dating techniques. Quat. Geochronol. 30, 90–99.

Song, Y., Luo, D., Du, J., Kang, S., Cheng, P., Fu, C., Guo, X., 2018. Radiometric dating of late quaternary loess in the northern piedmont of South Tianshan mountains: Implications for reliable dating. Geol J 53 (S2), 417–426.

Souza, P.E., Sohbati, R., Murray, A.S., Clemmensen, L.B., Kroon, A., Nielsen, L., 2021. Optical dating of cobble surfaces determines the chronology of Holocene beach ridges in Greenland. Boreas 50 (2), 606–618.

Souza, P.E., Sohbati, R., Murray, A.S., Kroon, A., Clemmensen, L.B., Hede, M.U., Nielsen, L., 2019. Luminescence dating of buried cobble surfaces from sandy beach ridges: A case study from Denmark. Boreas 48 (4), 841–855.

Talamo, S., Aldeias, V., Goldberg, P., Chiotti, L., Dibble, H.L., Guérin, G., Hublin, J.-J., Madelaine, S., Maria, R., Sandgathe, D., Steele, T.E., Turq, A., Mcpherron, S.J.P., 2020. The new 14C chronology for the Palaeolithic site of La Ferrassie, France: The disappearance of Neanderthals and the arrival of Homo sapiens in France. J. Quat. Sci. 35 (7), 961–973.

Thomsen, K.J., Murray, A.S., Bøtter-Jensen, L., Kinahan, J., 2007. Determination of burial dose in incompletely bleached fluvial samples using single grains of quartz. Radiat. Meas. 42, 370–379.

Thomsen, K.J., Murray, A.S., Buylaert, J.-P., Jain, M., Helt-Hansen, J., Aubry, T., 2016. Testing single-grain quartz OSL methods using known age samples from the Bordes-Fitte rockshelter (Roches d'abilly site, Central France). Quat. Geochronol. 31, 77–96.

Vafiadou, A., Murray, A., Liritzis, I., 2007. Optically stimulated luminescence (OSL) dating investigations of rock and underlying soil from three case studies. J. Archael. Sci. 34 (10), 1659–1669.

Vandenberghe, D., De Corte, F., Buylaert, J.-P., Kučera, J., 2008. On the internal radioactivity in quartz. Radiat. Meas. 43 (2–6), 771–775.

Vieillevigne, E., Guibert, P., Rita Zuccarello, A., Bechtel, F., 2006. The potential of optically stimulated luminescence for medieval building; A case study at Termez, Uzbekistan. Radiat. Meas. 41 (7), 991–994, Proceedings of the 11th International Conference on Luminescence and Electron-Spin Resonance Dating (LED 2005).

Wintle, A.G., Murray, A.S., 2006. A review of quartz optically stimulated luminescence characteristics and their relevance in single-aliquot regeneration dating protocols. Radiat. Meas. 41, 369–391.

Zilhão, J., Angelucci, D.E., Arnold, L.J., d'Errico, F., Dayet, L., Demuro, M., Deschamps, M., Fewlass, H., Gomes, L., Linscott, B., Matias, H., Pike, A.W.G., Steier, P., Talamo, S., Wild, E.M., 2021. Revisiting the middle and upper palaeolithic archaeology of gruta do caldeirão (Tomar, Portugal). PLoS One 16 (10), 1–65.